THE UNIVERSITY OF CHICAGO

FACETED WRINKLING AT A CONTRACTED CURVED BOUNDARY: ISOMETRY AND HYSTERETIC WAVELENGTH SELECTION

A DISSERTATION SUBMITTED TO
THE FACULTY OF THE DIVISION OF THE PHYSICAL SCIENCES
IN CANDIDACY FOR THE DEGREE OF
DOCTOR OF PHILOSOPHY

DEPARTMENT OF PHYSICS

BY
ANSHUMAN SANKAR PAL

CHICAGO, ILLINOIS
JUNE 2023

Contents

List of Figures

List of Tables

Abstract

Thin elastic sheets buckle to form a wide variety of morphologies that can be broadly categorised into two groups: smoothly wrinkled shapes, and sharply faceted shapes. According to common knowledge, the former is energetically dominated by external sources of work (like a substrate or boundary tension), while the latter is dominated by sources of work arising from the sheet's intrinsic elasticity and geometry. In this thesis, we analyse a buckled morphology that shows characteristics of both these aforementioned categories. We call this intermediate category *"faceted wrinkling"*. Using numerical finite-element simulations, we study a minimal two-dimensional system: a circular annulus contracted at the inner boundary by fraction Δ, so that it buckles into a radial wrinkling pattern that shows sharp zig-zag faceting at the inner boundary. In our first result, we argue that this morphology results from the fact that the wrinkling is asymptotically *isometric*, i.e. its stretching energy approaches zero relative to its bending energy. To this end, we compare our numerically generated solutions to an *Ansatz* zero-thickness solution made up of alternating triangles and cones that is developable, and hence isometric, by design. We find this isometric cone-triangle *Ansatz* to agree with simulations over a wide range of values of system size, thickness, and wrinkle wavenumber and amplitude. In our second result, we address the mechanism that selects the wrinkle wavelength λ in such a pure-bending configuration. Usually, wavelength selection in elastic wrinkling occurs through macroscopic competition between the sheet's bending energy and some external source of deformation work, like a (real or effective) substrate. What could select λ in the absence of any competition to the bending energy? Using our numerical simulations, we argue that competition between stretching and bending energies at mesoscopic scales leads to the selection of a wavelength scale sensitive to both the width w and thickness t of the sheet: $\lambda^* \sim w^{2/3} t^{1/3} \Delta^{-1/6}$. This scale λ^* corresponds to an arrest criterion for wrinkle coarsening in the sheet starting from any wavelength finer than λ^*: $\lambda \lesssim \lambda^*$. However, the sheet can support coarser wavelengths, $\lambda \gtrsim \lambda^*$, since there is no penalty to their existence. Since this wavelength selection mechanism depends on the initial λ, it is path-dependent (or hysteretic).

Preface

This thesis is an examination of the mechanics and pattern selection in the so-called "inner Lamé" wrinkling deformation, using a combination of theory and simulation. The thesis reproduces two papers: [1] and [2], that have been submitted to the journals *PNAS* (Proceedings of the National Academy of Sciences) and *Soft Matter* respectively. These papers have been reformatted for inclusion in the thesis, but are otherwise unchanged. The two papers are preceded by an introductory chapter that delineates (i) the larger scope of the thesis – namely, pattern formation in thin elastic sheets and the key role played by isometries in understanding them – and (ii) the principal features of thin sheet elasticity – viz. the thickness-mediated competition between bending and stretching modes, and the role played by intrinsic geometry. These topics are developed summarily, without many equations, and only to the point necessary for understanding and appreciating the thesis. They are based on inputs from textbooks and review papers, the informative commentary article by S. Venkatramani on elastic pattern formation [3], and on the detailed comments provided in the referee report to [1], supplemented by my own knowledge.

Chapters II and III contain the contents of the two papers [1] and [2], dealing with two almost-independent facets of this system: shape selection and wavelength selection. Chapter II, based on [1], deals with the logically prior question of how the wrinkling morphology is determined by macroscopic energy minimisation. The source paper [1] was co-authored by myself, Luka Pocivavsek (LP) and Thomas Witten (TW). It was submitted to *PNAS* and is currently in revision. In this work, I was responsible for selecting the system and guessing its significance, performing simulations and measurements, and for creating the main text and figures of the paper. LP was key in providing numerical support and in revising the paper. TW's contribution was to postulate the cone-triangle ansatz solution, to clarify many aspects of the theory and its shortcomings, to help in interpreting numerical results, and to revise and suggest text for the paper.

Chapter III, based on [2], deals with the enigmatic question of how a wavelength is selected in an unsupported sheet with only bending energy. Reference [2] was authored solely by me and is almost entirely my own work, in particular, guessing the non-trivial wavelength selection mechanism, and confirming it through simulations and measurements. Thomas Witten played a mentor's role in this process, acting as a sounding board, providing key physical insights, and aiding in the revision of the paper, helping to make it clear and cogent. It is currently under peer review.

References

[1] A. S. Pal, L. Pocivavsek, and T. A. Witten, *Faceted wrinkling by contracting a curved boundary*, 2022.

[2] A. S. Pal, *Hysteretic wavelength selection in isometric, unsupported radial wrinkling*, Nov. 2022.

[3] S. C. Venkataramani, "Buckling sheets open a door to understanding self-organization in soft matter", Proceedings of the National Academy of Sciences **116**, 1477–1479 (2019).

Chapter 1

Introduction and Overview

1.1 Thin elastic sheets: a model for soft matter self-organisation

This thesis on thin elastic sheets is situated within the larger domain of *soft condensed matter* (or 'soft matter"), a relatively recent branch of physics that studies matter that deforms significantly (hence the word 'soft').[1] More specifically, it concerns "materials in states of matter that are neither simple liquids nor crystalline solids of the type studied in other branches of solid state physics" [2], i.e. in some way lie between the traditional fields of solid state physics and fluids. Traditional soft matter systems live at micron scale or below ($\lesssim 10^{-6}$), though they can extend to the macroscopic scale as well (as we will see for thin sheets). Thus, soft matter as a field studies things that we can see and touch, and which even make up our bodies.

To a physicist, the interest of soft matter lies in the immense degree of *complexity* of the systems under study, which include liquid crystals, polymers, gels, colloids, complex fluids, etc. [2–4]. These systems are exemplars of what P.W. Anderson famously called "more is different", i.e. where the large-scale, macroscopic behaviour of properties are highly non-trivial functions of the constituent microscopic units, depending strongly on their geometry, dimensionality, connectivity/topology and mutual interactions [2]. In fact, soft matter systems even display what is known as 'multi-scale physics', in which interaction between microscopic units (usually at the atomic, molecular or micron scales) leads to the spontaneous creation of order and structure [2] – and new 'emergent' degrees of freedom – at intermediate

---

[1] This section, as well as Secs. 1.4 and 1.5, are inspired by S. Venkataramani's excellent commentary article [1].

[2] This is also known as 'self-assembly' or 'self-organisation'

‘mesoscopic’ scales. Often, one can get multiple iterations of this phenomenon, with emergent degrees of freedom at some mesoscopic scale interacting between themselves to create emergent structures at a larger mesoscopic scale, and so on hierarchically, before we finally reach the macroscopic scale. Oftentimes, soft matter systems are also subject to random thermal motion (hence, entropy), complicating things further. To get a good idea of exactly how rich and complex soft matter systems can get, we refer the reader to the physics of polymer systems [5, 6].

Among the many possible complex soft matter systems, thin elastic sheets or membranes stand out for their simplicity. They display a rich diversity of physical morphologies, despite having a very simple physical structure consisting of just a few ingredients. For example, from the outset, elasticity theory is a *coarse-grained*, continuum mechanical theory that ignores the existence of the constituent ‘particles’ of a material. All material particularities are captured in a few numerical constants, viz. the elastic moduli/stiffnesses. Indeed, for a uniform, isotropic, linearly elastic material, there are only *two* independent elastic moduli [7]. Next, in terms of spatial complexity, the possibility of having many length scales is limited. 3-dimensional (3d) bulk elasticity is particularly simple in this respect, since the entire macroscopic system can be described using only one geometric length scale: the system size L. As we reduce the dimensionality of the object to 2 or 1 dimensions (2d and 1d resp.), we isolate another dimension, the thickness $t \ll L$, which forms a new ‘microscopic’ or minimum length scale in the system. Thus, slender elastic objects – viz. one-dimensional (1d) rods and two-dimensional (2d) sheets – are characterised by only these two continuum length scales: t and L (with $t \ll L$). Finally, since there are no constituent microscopic particles involved, there is no question of having temperature or entropy in this physics. Despite this simplicity in description, thin elastic sheets [3] buckle and bend into a rich variety of highly deformed shapes (see Fig. 1.1) with fascinating physical properties, all of which can be studied with relatively simple tools from physics and geometry. Thus, thin elastic sheets may be viewed as a model system to build universal intuition about the coarse-grained energy mechanisms [4] underlying pattern formation and self-organisation in disparate macroscopic and soft matter physics systems.

---

[3] Thin one-dimensional rods, in comparison, are less rich and complex. We explain this in detail later.

[4] Coarse-graining, by its nature, emphasises universality.

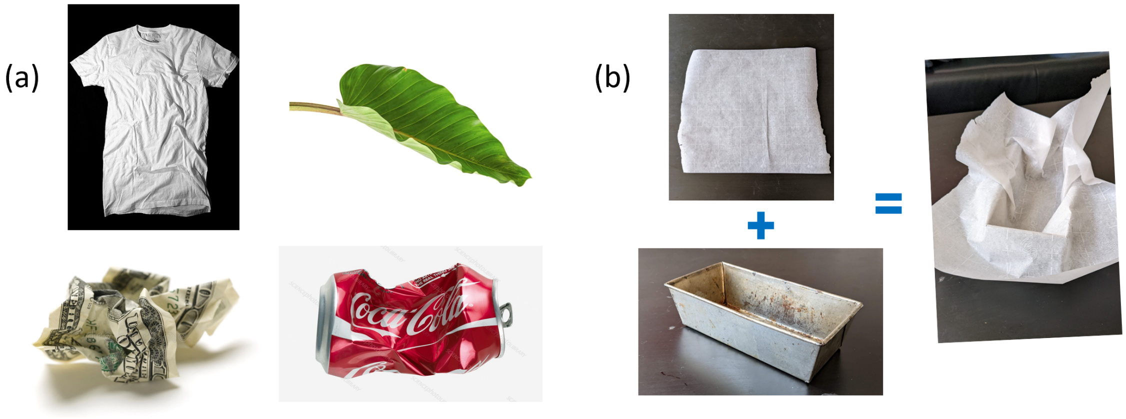

Figure 1.1: Example shapes and patterns formed through spontaneous bending of thin elastic sheets under compression and confinement. (a) Everyday patterns: (clockwise from top-left) a wrinkled t-shirt, a curly leaf, a crushed soda can, and a crumpled currency note. (b) shows an example of elastic pattern formation resulting from geometric incompatibility between objects. If we try to line a stiff, metallic baking pan with a flat sheet of parchment paper, the result is the randomly crumpled and wrinkled pattern seen on the right.

1.2 Seeking isometries: a fundamental question in thin sheet elasticity

The field of elasticity studies the *deformations* of solid objects, i.e. *changes in shape* through stretching and bending. As explained in the previous section, in this thesis, we are concerned with continuum elasticity, i.e. the study of continuous objects, generally understood to be at the macroscopic, human level. In particular, because of their fascinating and exotic behaviour, we are interested in two-dimensional (2d) elastic thin sheets.

A good, everyday example of an elastic sheet is a sheet of paper. A thin sheet, by virtue of its thinness (explained later in Sec. 1.4), bends very easily, and thus forms three-dimensional (3d) shapes [5]. Such bending can be generated manually, as in the art of origami or paper-folding, or can be generated spontaneously under some form compression/confinement, as in the example patterns and morphologies shown in Fig. 1.1. A fundamental question one can then ask is:

What are the shapes that a flat elastic sheet may form by bending?

As one might guess, one can *not* form any arbitrary shape with a flat sheet. To see this, consider the following example (see Fig. 1.1b). When a baker is trying to line a stiff metallic

---

[5] Mathematically, these are known as *embeddings* of the sheet's surface.

bread pan with parchment paper, they are asking the question: can the flat sheet take the shape of the bread pan? As soon becomes evident, the answer is no: the paper wrinkles and crumples in many ways, but refuses to take on the shape of the pan. The reason this happens is because the flatness of the sheet is fundamentally incompatible with the shape of the bread pan. The intrinsic *lengths* in the two shapes are different: at some places, there is more material between two adjacent points in the sheet as compared to two adjacent points in the pan. This mismatch in lengths (or 'geometric incompatibility') means that the parchment paper must compress in order to conform to the shape of the pan. However, as we explain later, thin sheets are extremely 'stiff' or resistant to stretching. Thus, the paper assumes a shape or configuration that is unstretched, but highly bent and conforming only very roughly to the shape of the pan.

This example shows us that the fundamental question above needs to be modified to the following:

> *What are the shapes that a flat elastic sheet may form by bending* without stretching?

Rephrasing this in mathematical terms: what are the *isometries* (from 'iso'=equal and 'metric'=length) of a flat sheet?[6] Some isometries readily come to mind, e.g. cylinders and cones. But these are too simple, in the sense that they provide no route to describe the variety of shapes observed in elastic pattern formation (c.f. Fig. 1.1), such as the baking pan liner above. Thus, what we are really looking for are *complex* isometries of a flat sheet. This is the question that animates the entirety of this work.

One may ask, why should one care about these isometries? The reasons are manifold. From a fundamental physics point of view, such spontaneously bent shapes (see again Fig. 1.1) represent vivid examples of self-organisation and pattern formation in nature under elastic forces, and thus merit study on their own basis. But beyond that, isometries are also of fundamental importance in natural and engineering design. Nature is known to use isometric design principles, since they allow transition between a flat and a folded state at little energy cost. This can be seen, e.g., in the bursting of pollen grains [11] and the infection of red blood cells by malarial parasites [12]. Similar ideas have also been exploited by human beings, for example, in the art of origami (literally, 'paper folding'), which can be used to make incredibly complex shapes [13, 14] as well as simple single-motion shapes such as large solar panels that can self-deploy robustly in outer space [15].

---

[6] One may pose the same question of sheets that are intrinsically spherical [8] or hyperbolic [9, 10]. But this work is only concerned with intrinsically flat sheets.

1.3 The "inner Lamé" system

In this dissertation, we study such a shape selection problem in a seemingly very simple system: a flat, unsupported circular annulus contracted radially at the inner boundary, so that it buckles to form a pattern of repeating radial wrinkles (see Fig. 1.2b). We name this the "inner Lamé" system [16]. While the 'loading' and overall geometry of the system are indeed very simple and symmetric, we will proceed to show that the selection of the final wrinkling pattern is a highly non-trivial processes, and consists of two separate processes:

1. *Shape selection*: the selection of the morphology of a single wrinkle (the 'unit cell'), and
2. *Wavelength selection*: the selection of the wrinkle length scale (equivalently, the number of wrinkles).

Using a combination of theory and numerical simulations, we will show that these two questions can only be answered taking into account some subtle features of the physics of thin sheets, in particular, i) their delicate interplay of stretching and bending energies, and ii) their strong geometric constraints. We also show that scale plays a big role in the answering of these two questions: the shape selection is determined by energetics at a global/macroscopic scale, whereas wavelength selection is determined by local energetics at a mesoscopic scale. Thus, this dissertation focuses mainly on the physical questions of how and why the matter self-organises into this particular shape. We also discuss possible applications of this physics in the design of deployable structures, and the possibilities of generalisation of these self-organisation mechanisms to other geometries.

1.3.1 Organisation of dissertation

The rest of the chapter is dedicated to providing background and context for our exploration of the physics of the inner Lamé system. In Sec. 1.4, we discuss the crucial interplay between cheap bending energy and expensive stretching energy, mediated by the thickness, that marks the physics of all slender elastic objects. In Sec. 1.5, we discuss the crucial role played by geometry and dimensionality in the elasticity of thin two-dimensional (2d) sheets. Finally, in Sec. 1.6, we focus back on the main theme of this thesis – the search for isometries of thin, flat sheets – and use the knowledge from Secs. 1.4 and 1.5 to briefly describe the two known categories of such isometries.

In Chapters II and III (and the appended articles [16] and [18] resp.), we discuss the original research of this dissertation. Each chapter addresses one of the two principal questions

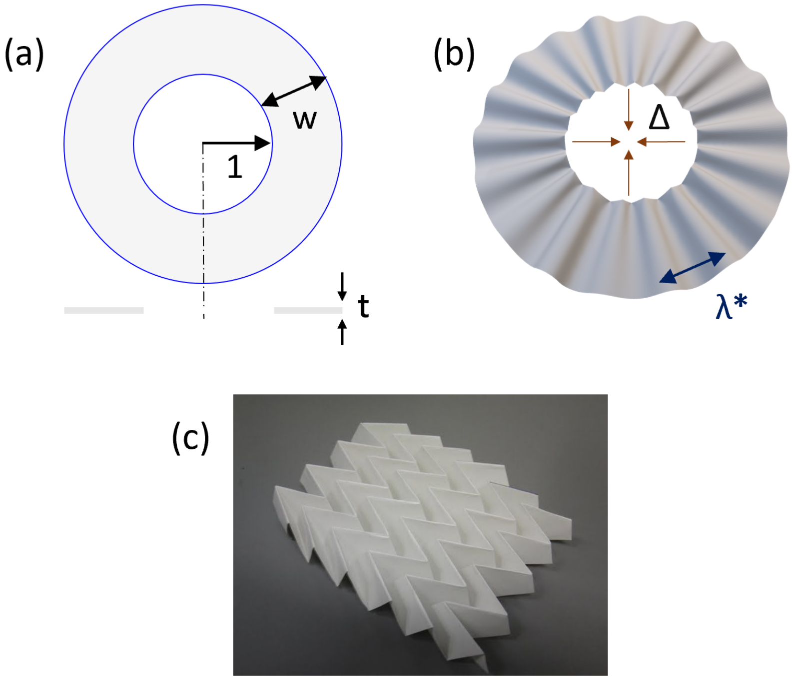

Figure 1.2: Geometry of the Inner Lamé radially wrinkled system. (a) A schematic diagram of the flat annulus, showing its geometric parameters: radial distance r, width w and (in cross-section) thickness t. We take the inner radius as unity. (b) An example of a deformed configuration, generated through finite-element simulation, showing the displacement Δ and the wrinkle wavelength λ^*, measured at the outer boundary. The inner boundary shows spontaneous zig-zag folding. This is reminiscent of the zig-zag folding found in Miura origami [15], like in the paper example shown in (c) [17].

that we are concerned with, respectively, *shape selection* and *wavelength selection*. In Chapter II, we argue that the geometry of the inner Lamé system allows it to assume a wrinkling morphology that is developable, and hence isometric, independent of thickness and amplitude. In other words, this wrinkling morphology is characterised by only the bending energy. Thus, we have extreme "energy imbalance" at the macroscopic level. On the other hand, in Chapter III, we claim that the selected wavelength (λ^* in Fig. 1.2) for the inner Lamé system emerges through "energy balance" at a mesoscopic level, by balancing stretching and bending energies in transient Y-shaped structures called 'wrinklons' [19] not present in the final shape. This leads to a special type of wavelength selection mechanism that is hysteretic.

1.4 Energy structure: the role of thickness

As stated in Section 1.2, slender elastic objects (both 1d rods and 2d sheets) are characterised by only two length scales - the 'microscopic' thickness t and the 'macroscopic' system size

L. This simplicity in the length structure of thin sheets is reflected in the simplicity of its deformation and energy structure as well. Deformations in slender objects an be categorised into one of *only two* almost-independent modes: stretching and bending.[7] Stretching refers to in-plane deformations of the material, leading to changes in material length. It is measured using dimensionless *strain*, i.e. the fractional change in length. Bending, on the other hand, refers to deformations normal to the plane ('out-of-plane') of the material. It is measured using the *curvature*, which has dimensions of 1/(length). While strain and curvature are both (symmetric) tensor quantities, their most fundamental scaling behaviour can be inferred considering only the relative magnitudes of these tensors. This suffices for our purposes.

Given the strain and curvature distributions, the total energy of elastic deformation (U_{elastic}) of a slender object can then be written as the linear sum of two separate contributions:

$$U_{\text{elastic}} = U_{\text{strain}} + U_{\text{bend}}, \tag{1.1}$$

where the global energies U_{strain} and U_{bend} are defined as the integrals (over the mid-plane of the material) of the local energy densities, which are proportional, respectively, to the square of the local strain and curvature. That is, they have the form:

$$U_{\text{strain}} \sim \frac{Y}{2} \int (\text{strain})^2 \tag{1.2}$$

$$U_{\text{bend}} \sim \frac{B}{2} \int (\text{curvature})^2, \tag{1.3}$$

involving integration over the length (in 1d) or area (in 2d). Here, the constants Y and B are, respectively, the stretching and bending stiffnesses[8], which capture all the dependence of the energy on material properties, as well as the object thickness. As with the stiffness of a single spring,[9] the stiffness of a mode determines the energetic cost of a unit deformation of the mode.

Ratios of stiffnesses and energies

Here and henceforth, we are interested in the equilibrium deformation or shape of an elastic object. This is given by the minimisation of the elastic energy U_{elastic}. A key ingredient of

---

[7] We will discuss in the next section how these two modes are not *fully* independent. But this point is only important in 2d.

[8] The *stiffness* is also referred to as the *modulus* or *rigidity*.

[9] Recall that for a single spring, we can write $U_{\text{elastic}} = \frac{k}{2}(l - l_0)^2$, where k is the spring's stiffness, l_0 is its equilibrium length and l is its current length. Thus, for unit deformation: $|l - l_0| = 1$, the energy is just half the stiffness: $U_{\text{elastic}} = \frac{k}{2}$.

the remarkably rich physics of thin sheets is the partition of energy between the parts U_{strain} and U_{bend}. This, in turn, is controlled by the thickness-mediated "separation of magnitude (or scale)" between the stretching and bending stiffnesses Y and B. For a slender object (i.e. a 1d rod or 2d sheet) of thickness t [20], the ratio of the two stiffnesses obeys the scaling relation:

$$B/Y \sim t^2, \tag{1.4}$$

a result that emerges from the integration over the thin dimension(s) required to reduce the 3d theory to 2d or 1d (see, e.g., [21]), but which can also be guessed from dimensional analysis. Eq. 1.4 implies that, if we consider two sheets of the same material having thicknesses t_1 and t_2 ($t_1 > t_2$), then the ratio B/Y for the thinner sheet is smaller than the B/Y for the thicker sheet by a factor of $(t_2/t_1)^2$.

To see the consequence of this for the energy ratio $U_{\mathrm{strain}}/U_{\mathrm{bend}}$, consider the following. The shape of a sheet is defined independently of its thickness. If a given shape has a given ratio $U_{\mathrm{strain}}/U_{\mathrm{bend}}$ at one thickness t_1, then that ratio for that same shape is increased as $(t_1/t_2)^2$ as the thickness decreases to t_2. Thus, for a sufficiently thin sheet, any deformation (i.e. change in shape) that reduces the strain energy can lower the total energy much more strongly than a deformation that reduces the bending energy. Thus, such strain-reducing deformations should be favoured over bending-reducing deformations in the thin sheet limit.

This argument tells us about the (relative) change in energies for a *fixed* shape. However, it does not determine the final equilibrium shape, nor the balance of energies $U_{\mathrm{strain}}/U_{\mathrm{bend}}$ in this state. We comment on these aspects next.

Equilibrium configuration and energy partition

The imbalance between the stretching stiffness Y and bending stiffness B (Eq. 1.4) can be used to highly simplify the task of finding the equilibrium (i.e. energy minimising) configuration, at least in simple systems like a 1d rod. For a thin rod, it suffices to directly take the infinitely-thin limit and impose zero stretching energy (i.e., zero strain) as a constraint while minimising only the bending energy.[10] This was done by Euler in his *Elastica* (1744) to accurately find the equilibrium shape of bent rods for a variety of boundary conditions [22].

---

[10] This is called the inextensible limit.

In 2d, however, things are more complicated due to the extra constraints placed by two-dimensional geometry, which make it difficult for a sheet to assume configurations where U_{bend} always dominates U_{strain}. For example, in a crumpled sheet of paper, the elastic energy is concentrated in singular structures called 'stretching ridges', where the stretching and bending energies are found to be in balance even in the zero-thickness limit, obeying a finite ratio: $U_{\text{strain}}/U_{\text{bend}} \to 1/5$ [23]. Thus, dimensionality and geometry add an extra ingredient that makes the search for isometries – i.e. configurations where $U_{\text{strain}}/U_{\text{bend}} \to 0$ as $t \to 0$ – in 2d fundamentally more complex.[11]

In the next sub-section, we discuss why and how geometry plays such an important role in two-dimensional (2d) thin sheet mechanics and pattern formation.

1.5 The role of geometry: 2d sheets vs. 1d rods

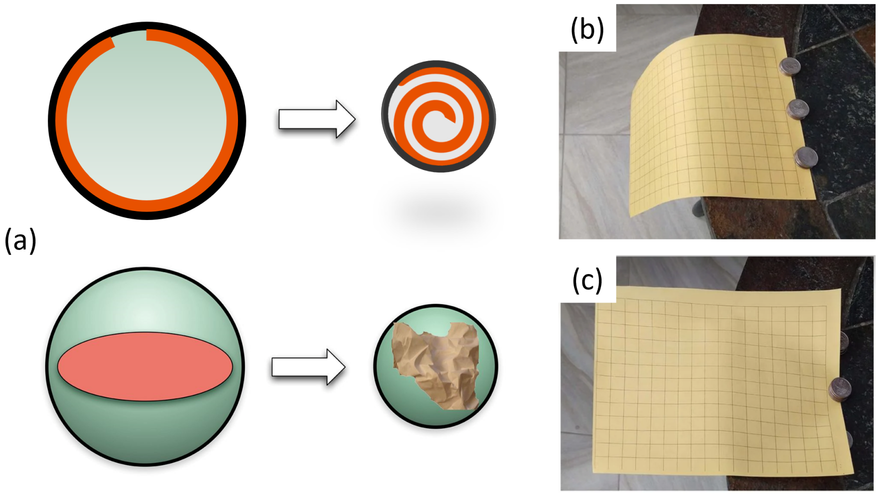

Figure 1.3: Illustrating the effect of geometry and dimensionality in the buckling of slender structures (figure adapted from [1]). (a) We compare a thin elastic (1d) rod that is confined by a ring in two dimensions and a thin elastic (2d) sheet that is confined by a sphere in three dimensions. The rod simply "curls up" following the boundary shape. The sheet, however, "crumples" into a ball-like shape with sharp, singular features. (b and c) A letter-size paper with a 1/2 inch grid is held by three stacks of five quarters, placed 2 inches apart. (b) The sheet is free to bend over the edge of the table without stretching since there is no curvature in the transverse direction. (c) Two of the stacks of quarters are now supporting the sheet from below to introduce a transverse curvature in the sheet. The sheet no longer bends over the edge, implying that the transverse curvature (somehow) imparts an extra longitudinal rigidity to the sheet.

---

[11] In other words, generalising Euler's *Elastica* to 2d is not a trivial task.

The discussions in the previous sections of this chapter have been mostly agnostic about the dimensionality of the slender object, and unless specified, have been equally valid for one-dimensional (1d) rods and two-dimensional (2d) sheets. That is because these discussions have been dependent only on the thickness t, as encapsulated in Eq. 1.4. In this section,[12] we show that this 'symmetry' between 1d and 2d systems is broken by geometry, in particular by Gauss' famous *Theorema Egregium*. This theorem, and the ideas contained therein, impart a new type of "geometric rigidity" to 2d sheets, rendering their pattern formation more complex, and hence more interesting.

A priori, the deformation space of a two-dimensional material should just be a simple product of two copies of the deformation space of a 1-dimensional material, i.e., a single stretching and bending direction should be replaceable by two perpendicular stretching and bending directions. Moreover, since stretching is an *in-plane* deformation, while bending is *out-of-plane*, they should *a priori* be independent deformation modes. However, reality is more complicated. In 1827, Carl Friedrich Gauss proved his famous geometric *Theorema Egregium*, which stated that stretching and bending in 2d are *not* fully independent modes. In other words, while the elastic energy can be expressed exactly as a sum of stretching and bending energies, the strain and curvature deformations that determine these energies *cannot* be independently varied in a real sheet. Thus, in general, a given shape and curvature profile cannot be achieved without some specific conditions on the strain profile.

In particular, the *Theorema* implies the following result:

Simultaneous bending in two independent directions requires stretching.

Since, as we have already seen, stretching is energetically very expensive for thin sheets, this means that double curvature in thin sheets is an expensive, and hence penalised, deformation. Gauss' *Theorema Egregium* thereby encodes an extra geometric constraint or rigidity in the mechanics of thin 2d sheets – one penalising double curvature – that is absent for 1d rods. This extra constraint is responsible for a complexity and diversity in the space of shapes and patterns produced by the bending of thin sheets that cannot be matched by rods. An illustrative example of this difference is provided in Fig. 1.3a. A thin rod confined inside a ring in two dimensions merely 'curls up' touching the boundary (overlapping itself if needed). However, a thin sheet confined inside a sphere in three dimensions cannot just conform to its doubly-curved surface. Instead, it forms a very complex 'crumpled' structure with flat facets and randomly distributed sharp ridges and points at scales much smaller than the system size.

---

[12] This section is also inspired by S. Venkataramani's opinion article [1].

The singular and jagged topography of the crumpled ball of paper is illustrative of a consequence of the geometric constraint encapsulated in Gauss' *Theorema* (1.5). From Eq. 1.4, we know stretching is expensive in a thin sheet. Then, considering the shape's change under a given confining geometry as the thickness goes to zero, any compound curvature in a given region would incur an arbitrarily large stretching energy penalty. This penalty can only avoided by eliminating compound curvature in the region. This property of having zero compound/Gaussian curvature is known as *developability* [24]. Developable shapes are characterised by the presence of straight lines in the material known as *directors* – corresponding at each point to the local principal direction of zero curvature – that can span the entire width of the material [25]. Such linear directors are what is responsible for the jagged appearance of a crumpled ball of paper.

Moreover, the role of these geometric director lines is not just cosmetic, but also functional. Since the straight directors cannot bend easily[13], they act as a source of non-local rigidity in the deformed sheet, strongly defining its shape as well as its mechanical response. This is illustrated in Figs. 1.3b,c. Here, by giving transverse curvature to a thin paper sheet, we generate straight directors in the longitudinal direction, which are rigid enough to support the sheet's weight. This is also known as the "pizza slice" example, since a similar tactic of using transverse curvature can be used to hold a pizza slice with one hand, without it flopping over at the far end.[14] The same idea of imparting rigidity through curvature is also used at the human scale, in building construction (e.g. with corrugated metal sheets) and in architecture (e.g. with paraboloid and hyperboloid shell structures) [26, 27].

1.6 Known categories of isometries

In Sec. 1.2, we discussed how the fundamental question animating this dissertation is the search for non-trivial *isometries* (or almost-isometries) of a flat sheet, i.e. deformations of the sheet that are free (or almost free) of strain. In terms of energies, we wish to find deformations of the flat sheet that have ratio $U_{\text{strain}}/U_{\text{bend}} \to 0$ as the sheet thickness $t \to 0$ (with respect to the system size or some macroscopic scale). This question is equivalent to finding a generalisation of Euler's *Elastica* to 2d systems, and its complexity arises from the intricate interplay of the two elastic energies discussed in Sec. 1.4, along with the geometric constraints discussed in Sec. 1.5.

---

[13] Again, because this would generate double curvature and hence expensive stretching.

[14] This will work provided the pizza slice is not too heavy. Otherwise, gravity will overcome the rigidity of the directors.

The past decade in particular has seen a rich vein of research in this direction. According to current understanding, such isometries can be classified into one of two broad categories. In this section, we provide a brief summary[15] of these two broad classes. The two categories of isometries can be separated not only visually – because of their strikingly different morphologies (see Fig. 1.4) – but also energetically – in terms of both energy partition and spatial distribution – and by the nature of their approach to the zero-thickness limit. This discussion will provide the immediate context for the novel inner Lamé morphology studied in this dissertation.[16]

1.6.1 Wrinkled "asymptotic isometries"

Following the discussion in Sec. 1.4, one evident approach to attaining isometry is simply to take the $t \to 0$ limit for some morphology. By this, we mean the following: we start with a given configuration generated at given thickness t for some given loading or confinement, and then gradually reduce the thickness to zero, holding the confinement fixed. Since this class of isometries only exists in the limit of zero thickness,[17] we refer to them as "asymptotic isometries" [28, 29, 35–37].[18] These asymptotic isometries are commonly seen in sheets subject to compression in the presence of a (real or effective) substrate, so that they buckle into *wrinkled* morphologies [28] – i.e. buckling into multiple smooth undulations with a wavelength usually denoted λ.[19]

The top row of Fig. 1.4 shows three images of a radially wrinkled configuration – from the same experiment – evolving as the sheet thickness is decreased. The experiment involves poking a thin polystyrene film floating on a water bath [29–31]. Such poking in the presence of radial surface tension generates compression in the azimuthal direction, which can be relieved through wrinkling. From left to right, the images show sheets of thickness (a) $t = 157nm$, (b) $t = 113nm$, and (c) $t = 40nm$, having approximately the same poking depth δ. As t decreases, we can see the wrinkle wavelength λ becoming finer and finer. Since a smaller λ implies stronger curvature and hence greater bending, this comparison suggests that bending deformations increase as the thickness decreases (for fixed poking

---

[15] For more details, please read the references. In particular, we recommend the review article [28].

[16] The author would like to thank the anonymous referee to [16] for clarifying several aspects of the discussion below.

[17] The $t \to 0$ limit for 1d rods is relatively simple, and is the subject of Euler's *Elastica*, as mentioned in Sec. 1.4

[18] The class of 'asymptotic isometries' involves taking another limit as well, that of small tensile loading [28]. This is essential to the definition, but inessential for the discussion here.

[19] Since the amplitude is determined by the wavelength λ in the thin, inextensible limit, a wrinkle deformation is fully characterised by λ.

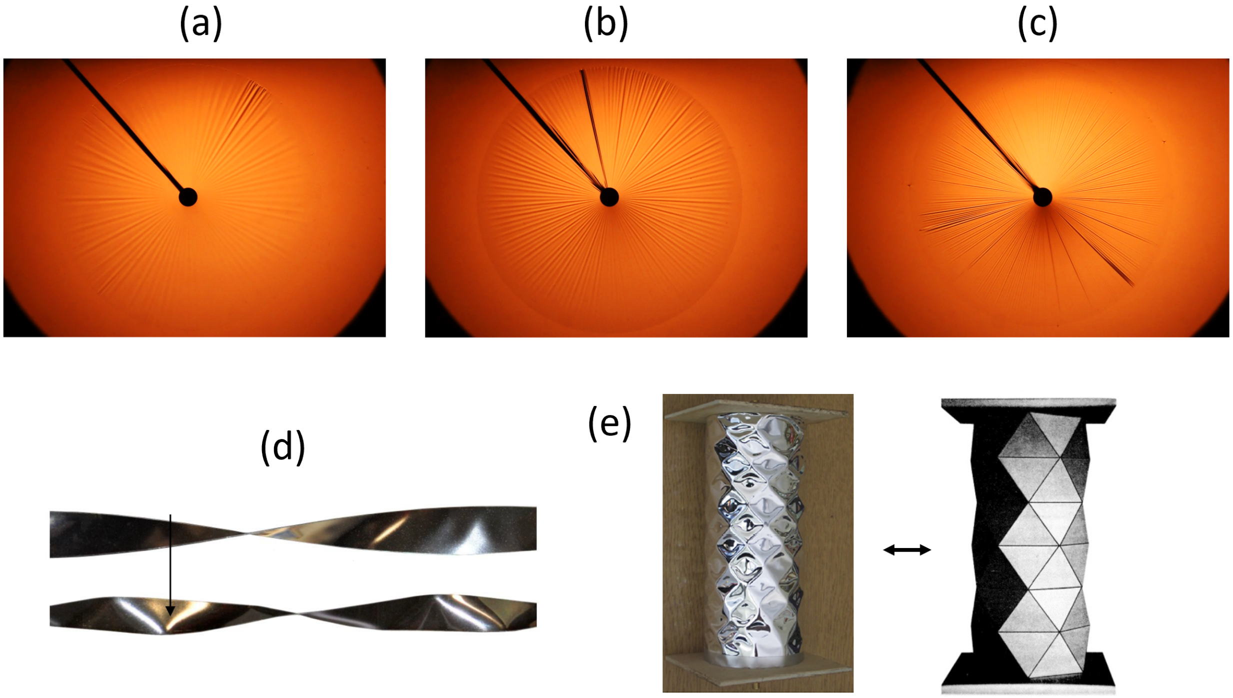

Figure 1.4: Illustrative examples of the two broad categories of thin sheet isometries discussed in Sec. 1.6. The top row shows photos (top views) of a radially wrinkled morphology that becomes 'asymptotically isometric' as the thickness is decreased. Here, a thin disk-like sheet floating on a water bath is poked with a metal rod [29, 30] (images modified from [31]). From left to right, the sheets have thicknesses t of a) 157nm, b) 113nm, c) 40nm. The black line is the shadow is of the poking rod. The poking depth is roughly the same in all three photos. We can see the wrinkle wavelength becoming finer as t decreases. In contrast, the bottom row shows examples of 'developable isometries', which show polygonal faceting. d) An elastic ribbon when twisted (without any longitudinal tension) buckles into a pattern of repeating triangular facets (image adapted from [32]). e) "Diamond buckling" in an axially compressed cylinder. (left) An experimental mylar sheet cylinder ($t \sim 10\mu m$) fitted onto a mandrel core (image from [33]). (right) Yoshimura's origami cylinder, created by folding a flat sheet along prescribed hinge lines, before joining the edges (image from [34])

distance). However, this does not tell us anything definitive about the energies. This point is addressed in later theoretical work by Vella, Davidovitch and colleagues [29, 30, 35–37]. They predict the wavelength λ to vanish in the zero-thickness limit as $\sqrt{t/\delta}$ – consistent with measurements – which implies that the energy ratio $U_{\text{strain}}/U_{\text{bend}}$ should also vanish in this limit, as expected for an isometry.

We highlight some identifying characteristics of this class of "wrinkly" isometries:

- First and foremost is its behaviour as we decrease the thickness and approach the $t \to 0$ limit. As the sheet gets thinner and thinner, the wrinkling wavelength λ becomes smaller and smaller without bound. Thus, there is no single configuration to which the sheet converges in the $t \to 0$ limit.
- Second, since the wrinkle amplitude is proportional to the wavelength in the inextensible thin-sheet regime, it also vanishes as $t \to 0$. In other words, the wrinkles become tinier and tinier in both height and width as the thickness decreases (for fixed loading or confinement).
- Third, the elastic energy (both bending and strain) is smoothly distributed over the entire sheet. This is in contrast to the "faceted isometries" of the next section, where the energy is inhomogeneously distributed in spatially localised "boundary layers". Henceforth, we refer to this smoothly distributed energy as 'macroscopic' or 'bulk' energy, to differentiate it from these boundary layers.

1.6.2 Faceted "developable isometries"

The second category of isometries differs fundamentally from the first category in that there is a specific target shape that the deformed sheet tends to as the sheet gets thinner and thinner. This target shape is determined by the constraints of geometry in the $t = 0$ limit. In view of the discussion in Sec. 1.5, the limiting isometric morphology must correspond to an "origami-like" (piecewise) developable surface, i.e. one with zero Gaussian curvature (see Fig. 1.4d). Thus, in contrast to the first 'asymptotic' category, this category of "developable isometries" explicitly exploits the geometric properties of 2d surfaces (as discussed in Sec. 1.5).[20]

Such developable isometries are usually seen in unconstrained sheets [28], i.e., sheets without any substrate or boundary tension or other external source of deformation work. Recall that developability means that there is a straight material line through every point of the

---

[20] This category of isometric deformations is thus unavailable to 1d systems.

surface, corresponding to the direction of zero principal curvature (see Sec. 1.5). Thus, these isometries are characterised by the presence of flat, polygonal *facets*, i.e. piecewise flat material regions, separated by sharp/jagged line-like or point-like singular features, respectively known as 'ridges' [7, 23] and 'd-cone tips' [38–40] in the literature. The bottom row of Fig. 1.4 presents examples of systems which buckle with spontaneously ordered faceting. In particular, Fig. 1.4d contrasts an experimentally obtained 'diamond buckling' morphology [33] with its putative geometric surface constructed through origami [34]. The crumpled ball of paper shown in Fig. 1.3a is instead an example of disordered faceting.

A big difference between this class of developable isometries and the previous 'wrinkly' class lies in its behaviour as we decrease the thickness and approach the $t \to 0$ limit. In terms of morphology, while wrinkly isometries have no limiting shape because of their diverging wavenumber, developable isometries show smooth convergence to the limiting shape given by the geometric (i.e., zero-thickness) developable surface. The main divergence from the $t = 0$ geometric surface, indeed, is restricted to narrow "boundary layers" concentrated at the line-like ridges and point-like conical singularities, whose size decreases to zero with the thickness (see the two images in Fig. 1.4d).

As a consequence, we can think of the sheet's morphology as being decomposable into a 'macroscopic' (or 'gross' or 'bulk') part covering almost all of the sheet's surface – which is determined by some $t = 0$ developable surface – and a finite set of 'mesoscopic' spatially-concentrated boundary layers, where the morphology differs from the $t = 0$ surface significantly. Thus, a significant feature of developable isometries is that, in terms of *gross* morphology, they show negligible change with changing thickness, and can thus be considered thickness-*independent*. On the other hand, because of the vanishing wavelength, the gross morphology of the asymptotic isometries can be said to be thickness-*dependent*.

Thus, the main effect of thickness for developable isometries is restricted to the small-scale boundary layers mentioned above. The sharp lines and points defined for the $t = 0$ geometric surface (see right image of Fig. 1.4d) have discontinuous curvature. At finite thickness, i.e. for finite bending modulus, such discontinuities would cost infinite bending energy. To avoid this, these discontinuities are "rounded off" at the expense of some non-zero stretching energy, localised to these boundary layers.[21] Thus, the boundary layers in the sheet are not only zones of discrepancy with the $t = 0$ limiting configuration, but

---

[21] Thus, stretching can exist in an otherwise-isometric sheet in these localised boundary layers of finite size.

also zones of concentrated energy. Furthermore, the macroscopic morphology is composed of flat and isometric facets, which have (comparatively) negligible stretching and bending energies. Thus, for ‘faceted isometries’, we conclude that the net macroscopic or bulk energy is effectively zero, and that all elastic energy effectively lives in these lower-dimensional line-like and point-like boundary layers [7]. This is thus in stark contrast to the ‘asymptotic isometry’ category, where the energy is uniformly distributed over the wrinkled surface. The contrasting spatial distributions of energy strongly influence the qualitatively different approaches to the zero-thickness limit for the two isometry categories.

	“Wrinkly” isometry	Faceted isometry	Faceted wrinkling
Target shape (as $t \to 0$)	Not defined	Defined	Defined
Deformation amplitude (as $t \to 0$)	Vanishes	Negligible change	Depends on initial conditions
Gross morphology (as $t \to 0$)	Changes	Negligible change	Depends on initial conditions
Bulk U_{bend} (at finite t)	Finite	Negligible	Finite
Bulk U_{strain} (at finite t)	Finite	Negligible	Negligible

Table 1.1: Salient properties of the two known existing categories of isometries (left and middle columns), and the new category proposed in this dissertation (right column).

1.6.3 The inner Lamé morphology: a new, intermediate category of isometry?

The discussion in this section serves as the perfect point to dive into the subject of this dissertation. In Chapter II, we will argue that the “faceted wrinkling” seen in our inner Lamé radially contracted annulus (Fig. 1.2) is a novel kind of isometry that shows aspects of both extant categories: it is developable and wrinkled at the same time. In particular, we posit that the $t = 0$ limiting wrinkled morphology is given by a piecewise developable surface made of alternating triangles and cones. Because of the presence of cones, the macroscopic/bulk energy consists of only bending energy and no stretching energy. Thus, we have $U_{\text{strain}}/U_{\text{bend}} \ll 1$ even at non-zero thickness (provided the wavelength does not vanish). This energy partition has strong consequences on the properties of the inner Lamé deformation.

It favours the restriction of this deformation to a robust, bending-only (locally) minimum-energy channel that avoids stretching, even up to very large amplitudes. This makes the inner Lamé deformation akin to the robust and reversible single-mode deformations seen in Miura-*ori* zig-zag pleated sheets [15], used as deployable structures.

However, wrinkling means that the sheet has also spontaneously selected some wavelength λ. In particular, our simulations suggest that the wavelength $\lambda \to 0$ as $t \to 0$ (along with the amplitude), much as for regular, smooth wrinkling. In the latter case, the wavelength is selected by competition between bending and competing external sources of work, like a (real or effective) substrate [30, 41–43]. But here, there is no such source of work present. Thus, the question is, what mechanism could be responsible for selecting λ? In Chapter III, we propose a mechanism in which energy balance between stretching and bending at local boundary layer-like scales selects a wavelength λ. This mechanism is *hysteretic* in that the final λ chosen depends on the initial conditions. Thus, the number of wrinkles m in the configuration ($m \sim 1/\lambda$) depends on the initial conditions and thickness t, but once this m is selected, the approach to the zero-thickness morphology happens as with other developable isometries.

References

[1] S. C. Venkataramani, "Buckling sheets open a door to understanding self-organization in soft matter", Proceedings of the National Academy of Sciences **116**, 1477–1479 (2019).

[2] R. A. L. Jones, *Soft condensed matter* (Oxford University Press, 2002), p. 195.

[3] M. Daoud and C. E. Williams, eds., *Soft matter physics* (Springer Berlin Heidelberg, 1999).

[4] T. A. Witten, *Structured fluids polymers, colloids, surfactants, Polymers, colloids, surfactants : xd-us* (Oxford University Press, 2010), p. 216.

[5] P. G. de Gennes, *Scaling concepts in polymer physics* (Cornell University Press, 1979), p. 324.

[6] M. Doi, *Introduction to polymer physics* (Clarendon Press, 1996), p. 120.

[7] T. A. Witten, "Stress focusing in elastic sheets", Reviews of Modern Physics **79**, 643–675 (2007).

[8] I. Tobasco, Y. Timounay, D. Todorova, G. C. Leggat, J. D. Paulsen, and E. Katifori, "Exact solutions for the wrinkle patterns of confined elastic shells", Nature Physics **18**, 1099–1104 (2022).

[9] E. Sharon, B. Roman, M. Marder, G.-S. Shin, and H. L. Swinney, "Buckling cascades in free sheets", Nature **419**, 579–579 (2002).

[10] K. K. Yamamoto, T. L. Shearman, E. J. Struckmeyer, J. A. Gemmer, and S. C. Venkataramani, "Nature's forms are frilly, flexible, and functional", The European Physical Journal E **44**, `10.1140/epje/s10189-021-00099-6` (2021).

[11] E. Katifori, S. Alben, E. Cerda, D. R. Nelson, and J. Dumais, "Foldable structures and the natural design of pollen grains", Proceedings of the National Academy of Sciences **107**, 7635–7639 (2010).

[12] A. Callan-Jones, O. E. Albarran Arriagada, G. Massiera, V. Lorman, and M. Abkarian, "Red blood cell membrane dynamics during malaria parasite egress", Biophysical Journal **103**, 2475–2483 (2012).

[13] R. J. Lang, *Origami design secrets mathematical methods for an ancient art, second edition, Mathematical methods for an ancient art, second edition* (A K Peters/CRC Press, 2011), p. 758.

[14] N. Turner, B. Goodwine, and M. Sen, "A review of origami applications in mechanical engineering", Proceedings of the Institution of Mechanical Engineers, Part C: Journal of Mechanical Engineering Science **230**, 2345–2362 (2015).

[15]K. Miura, “Method of packaging and deployment of large membranes in space”, The Institute of Space and Astronautical Science report, 1–9 (1985).

[16]A. S. Pal, L. Pocivavsek, and T. A. Witten, *Faceted wrinkling by contracting a curved boundary*, 2022.

[17]A. Benincasa, *The miura fold [pinterest post]*, Pinterest, Retrieved March 23, 2023, n.d.

[18]A. S. Pal, *Hysteretic wavelength selection in isometric, unsupported radial wrinkling*, Nov. 2022.

[19]H. Vandeparre, M. Piñeirua, F. Brau, B. Roman, J. Bico, C. Gay, W. Bao, C. N. Lau, P. M. Reis, and P. Damman, “Wrinkling Hierarchy in Constrained Thin Sheets from Suspended Graphene to Curtains”, Physical Review Letters **106**, 224301 (2011).

[20]B. Davidovitch, “Lectures on elasto-capillarity: 2017 summer school on soft solids and complex fluids (umass amherst)”, May 2017.

[21]B. Audoly and Y. Pomeau, *Elasticity and geometry* (OUP Oxford, Jan. 2010).

[22]R. Levien, *The elastica: a mathematical history*, tech. rep. UCB/EECS-2008-103 (EECS Department, University of California, Berkeley, Aug. 2008).

[23]A. Lobkovsky, S. Gentges, H. Li, D. Morse, and T. A. Witten, “Scaling Properties of Stretching Ridges in a Crumpled Elastic Sheet”, Science **270**, 1482–1485 (1995).

[24]M. P. do Carmo, *Differential Geometry of Curves & Surfaces* (Prentice Hall, 1976).

[25]S. C. Venkataramani, T. A. Witten, E. M. Kramer, and R. P. Geroch, “Limitations on the smooth confinement of an unstretchable manifold”, Journal of Mathematical Physics **41**, 5107–5128 (2000).

[26]A. Bhatia, *How a 19th century math genius taught us the best way to hold a pizza slice*, (2014) `https://www.wired.com/2014/09/curvature-and-strength-empzeal/` (visited on 10/03/2022).

[27]H. Pottmann, A. Asperl, M. Hofer, and A. Kilian, *Architectural geometry* (Bentley Institute Press, 2007), p. 744.

[28]J. D. Paulsen, “Wrapping liquids, solids, and gases in thin sheets”, Annual Review of Condensed Matter Physics **10**, 431–450 (2019).

[29]D. Vella, J. Huang, N. Menon, T. P. Russell, and B. Davidovitch, “Indentation of Ultrathin Elastic Films and the Emergence of Asymptotic Isometry”, Physical Review Letters **114**, 014301 (2015).

[30] J. D. Paulsen, E. Hohlfeld, H. King, J. Huang, Z. Qiu, T. P. Russell, N. Menon, D. Vella, and B. Davidovitch, “Curvature-induced stiffness and the spatial variation of wavelength in wrinkled sheets”, Proceedings of the National Academy of Sciences **113**, 1144–1149 (2016).

[31] N. Menon, *Private communication.*

[32] H. Pham Dinh, V. Démery, B. Davidovitch, F. Brau, and P. Damman, “From Cylindrical to Stretching Ridges and Wrinkles in Twisted Ribbons”, Physical Review Letters **117**, 104301 (2016).

[33] K. A. Seffen and S. V. Stott, “Surface texturing through cylinder buckling”, Journal of Applied Mechanics **81**, `10.1115/1.4026331` (2014).

[34] G. W. Hunt and I. Ario, “Twist buckling and the foldable cylinder: an exercise in origami”, International Journal of Non-Linear Mechanics **40**, 833–843 (2005).

[35] D. Vella, H. Ebrahimi, A. Vaziri, and B. Davidovitch, “Wrinkling reveals a new isometry of pressurized elastic shells”, EPL (Europhysics Letters) **112**, 24007 (2015).

[36] D. Vella and B. Davidovitch, “Regimes of wrinkling in an indented floating elastic sheet”, Physical Review E **98**, `10.1103/physreve.98.013003` (2018).

[37] B. Davidovitch, Y. Sun, and G. M. Grason, “Geometrically incompatible confinement of solids”, Proceedings of the National Academy of Sciences **116**, 1483–1488 (2019).

[38] E. Cerda and L. Mahadevan, “Conical Surfaces and Crescent Singularities in Crumpled Sheets”, Physical Review Letters **80**, 2358–2361 (1998).

[39] E. Cerda, S. Chaieb, F. Melo, and L. Mahadevan, “Conical dislocations in crumpling”, Nature **401**, 46–49 (1999).

[40] E. Cerda and L. Mahadevan, “Confined developable elastic surfaces: cylinders, cones and the elastica”, Proceedings of the Royal Society A: Mathematical, Physical and Engineering Sciences **461**, 671–700 (2005).

[41] E. Cerda and L. Mahadevan, “Geometry and Physics of Wrinkling”, Physical Review Letters **90**, 074302 (2003).

[42] B. Davidovitch, R. D. Schroll, D. Vella, M. Adda-Bedia, and E. A. Cerda, “Prototypical model for tensional wrinkling in thin sheets”, Proceedings of the National Academy of Sciences **108**, 18227–18232 (2011).

[43] F. Box, D. O’Kiely, O. Kodio, M. Inizan, A. A. Castrejón-Pita, and D. Vella, “Dynamics of wrinkling in ultrathin elastic sheets”, Proceedings of the National Academy of Sciences **116**, 20875–20880 (2019).

Chapter 2

The inner Lamé system: isometric radial wrinkling

This chapter is a reproduction of the article "*Faceted wrinkling by contracting a curved boundary*", authored by Anshuman S. Pal, Luka Pocivavsek and Thomas A. Witten. The preprint is available at `https://arxiv.org/abs/2206.03552`. The article is currently under peer review at the journal *Proceedings of the National Academy of Sciences (PNAS)*. This chapter reproduces a version of the article that has been significantly revised in response to referee comments; further minor revisions have been made to adapt it to thesis format. The paper also contains a significant *Supplementary Information (SI)* section, that has been included here in Sec. 2.7. For the contributions of the co-authors to the article, please refer to the *Preface* of this dissertation.

Abstract

Single-mode deformations of two-dimensional materials, such as the Miura-*ori* zig-zag fold, are important to the design of deployable structures because of their robustness, but usually require careful pre-patterning of the material. Here, we show that inward contraction of a curved boundary produces a novel single-mode deformation without any pre-patterning. Using finite-element representation of the contraction of a thin circular annular sheet, we show that these sheets wrinkle into a structure with negligible stretching energy, in which the contracted boundary forms spontaneous facets. We construct a strictly isometric wrinkled surface formed of triangles and cones that matches geometric and energy features closely,

suggesting that this class of partly-faceted wrinkled deformations is isometric. Isometry favours the restriction of such deformations to a robust low-bending energy channel that avoids stretching. This class of buckling also offers a novel way to manipulate sheet morphology via boundary forces. Finally, it serves as a minimal model for illustrating the strong constraints imposed by geometry in elastic pattern formation.

2.1 Introduction

The flourishing field of extreme mechanics [1–4] seeks ways in which large, spontaneous material deformations yield robust, reproducible structures and motions. Many of these structures exploit the selective deformations shown by thin sheets, which bend or fold easily but resist internal stretching strongly [5–16]. The large resistance to stretching creates strong, non-local constraints that restrict the sheet to selected modes of deformation. A classic example is the Miura-*ori* folding pattern [17–19]. This periodic pattern enables to contract a spread-out flat sheet of paper into a compactly folded state with one single mode of deformation dictated by the pattern (see Fig. 2.1a). Here we report similar robust deformation of a flat sheet without the position-dependent processing needed for an origami fold. Instead, we specify an initial annular shape and a simple mode of *edge* deformation: contracting the inner boundary radially. The result is a strongly reproducible three-dimensional pattern of high-amplitude wrinkles. We attribute the reproducibility to a qualitative feature of the simulated, finite-element simulation—each wrinkle approaches an isometric shape, with no stretching. This unstretched morphology is made possible by a distinct pattern of flat, triangular facets alternating with smoothly-curving conical segments.

We consider a minimal form of radial contraction that we call “inner Lamé” contraction. We displace the inner boundary of the annulus with no further constraints. As shown in Fig. 2.1c, this contraction produces fine wrinkling like the conventional Lamé contraction of Fig. 2.1b. However the two wrinkled states are radically different. The conventional Lamé wrinkle wavelength is explained in terms of the applied tension [20]. However, in the inner Lamé, the exterior tension of the Lamé state is absent, and so the established mechanism for the wrinkle wavelength cannot apply. Indeed, our wrinkling contrasts with most wrinkled systems, where the bending energy favoring longer wavelengths is countered by the energy associated with some external forcing [9, 21]. The wrinkle wavelength then depends explicitly on the strength of this constraint. The inner Lamé system has no such strength parameter. Instead, the deformation is defined in terms of the geometric displacement of the inner edge only.

Even among geometrically-defined forms of wrinkling, the inner-Lamé geometry is anoma-

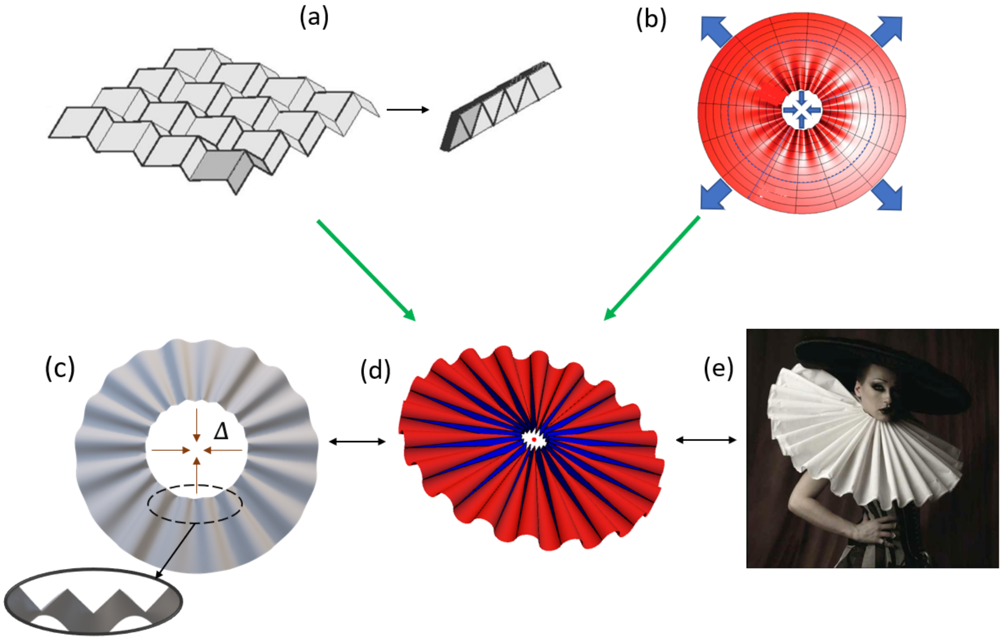

Figure 2.1: Geometry-controlled robust radial wrinkling. a) Miura-*ori* patterns guide a flat sheet to contract into a folded state with a single, continuous motion (adapted from [19]). b) Smooth radial (i.e., Lamé) wrinkling in an annulus under both inner and outer tension, indicated by arrows (adapted from [20]). In this paper, we study Miura-*ori* like robust deformation of an annulus in a radial Lamé setting. This deformation can be generated in multiple ways. c) Finite-element calculated shape under uniform radial contraction of the inner boundary, described in *Methods* (inset shows detail of emergent zigzag inner boundary). d) Circular-cone-triangle geometric construction defined in Sec. 2.3, with triangles shown in blue and cones in red. e) Ruff collar garment (source: internet) made by manually pleating the inner boundary of an annular piece of cloth.

lous. It doesn't conform to typical one-dimensional buckling treatable as an Euler elastica system [22]. Other forms in which the constraint is applied at one boundary [14, 23] do not give a well-defined wave number as we find.

We note that the forms of wrinkling mentioned above are explained as equilibrium ground-states of the system. In our system the wrinkles emerge from a quasistatic deformation. That is, the inner displacement is applied gradually, and the configuration is allowed to relax at every stage. This procedure corresponds to how one would perform the deformation experimentally. In this limit, the system follows a given energy minimum as the deformation is imposed. It need not be an energy ground state.

In this paper we address the structure of the individual wrinkles resulting from this unusual mode of deformation. Understanding this structure seems prerequisite to accounting for the wrinkle wavelength. We show that a strain-free isometric shape quantitatively accounts for observed features of our simulated shape. Specifically, the simulated deformation matches an explicitly isometric deformation of the original annulus into a cone-triangle pattern. We describe the robustness of the structure using a variety of initial and boundary conditions for the contracted inner boundary. We argue that the observed robustness of the cone-triangle structure is a natural consequence of its isometric property. We note how the cone-triangle structure can be induced via different paths, as illustrated in Figs. 2.1c, d, and e, and discuss generalisations to a broader range of structures. Using the findings of this paper, we address the wavelength question in a separate work [24].

Sections 2.2 and 2.3 define the inner Lamé deformation that we simulate, and the isometric model shape used for comparison. In Section 2.4, we show that the shape and energy of the simulated sheet are consistent with the model. Finally, Section 2.5 addresses our assumptions and discusses the value of such deformations for generating spontaneous structures.

2.2 Inner Lamé deformation

Given the circular annulus of Fig. 2.2a, we define the inner Lamé deformation as the equilibrium shape induced by drawing the inner boundary inward by a distance Δ, so that it is forced to live on a cylinder whose radius is reduced by Δ.[1] We define the initial inner radius as our unit of length. The pull distance Δ thus acts as the sole loading parameter in the system. The system can thus be conveniently defined using only three geometric parameters: thickness t, the width w, and displacement 'loading' Δ. The internal forces determining the shape arise from the bending modulus B, and the in-plane stretching modulus Y. In thin sheets with thickness t much smaller than the inner radius and the width w, the sheet may be taken as virtually unstretchable, and many features of the shape are independent of Y [7, 20].

We may anticipate that this inner Lamé deformation is strictly isometric by using the post-buckling far-from-threshold (FT) analysis of ref. [20] for the classic Lamé problem, where tension is applied at *both* the inner and outer boundaries. In the FT regime, the wrinkling slopes grow to the order of unity, and the associated azimuthal stress becomes negligible compared to the pre-buckling stress. Only the *bending azimuthal stress*, owing to wrinkling, proportional to the bending modulus and the curvature, remains. The same is expected for our inner Lamé case: consider the radial stress in a narrow sector of the annulus (see Fig. 2.2c). Equilibrium requires that the net radial force on the sector be zero. In the unbuckled state, the inner tension driving the deformation is balanced by the net

---

[1] As discussed in Sec. 2.5, we constrain the inner boundary to move only parallel to the axis of the cylinder.

outward component of the azimuthal stresses on the sides of the sector. But in the FT regime, this stress is negligible, as argued above. In addition, there is no radial tension at the outer boundary. We conclude that the only forces to balance the inner tension are the weak bending stresses.

The absence of any deformation stress except for bending stress would imply that the deformed sheet deforms only by bending in the thin limit. That is, it is isometric to the undeformed flat annulus. Such a limit can be attained by wrinkles of diverging fineness [6, 16]. But if a limiting shape of finite wavevector is to exist, then it must obey the geometrical property of "developability". That is, in view of Gauss's Theorema Egregium [25] there must be a straight generator line through each point of the surface that extends to the boundary without curving in space [26] In the next sections, we show that the contracted annulus is indeed consistent with a specific developable surface, suggested by the numerically determined shape.

2.3 A developable cone-triangle model

The faceted inner Lamé morphology of Fig. 1 suggests a further hypothesis: that the wrinkled morphology can be seen as a piecewise union of alternating flat triangles and curved cones. We take this as the starting point for our geometric model. For a configuration with wavenumber m, we consider a flat configuration (see Fig. 2.2b) where the inner boundary is a $2m$-sided polygon. Each segment of this boundary is the base of an isosceles triangle of height w. To complete the annulus, the apexes of adjacent triangles are joined with an arc. The constructed surface then consists of these triangles and the sectors joining them.

One may readily specify an isometric deformation that allows the inner boundary of this structure to contract. We deform the initial surface by translating the base of each triangle inward toward the centre, specifying that the triangles remain rigid. In order to maintain their shape and connectivity, the triangles must tilt (i.e. rotate about their midlines) increasingly as they are drawn inward; adjacent triangles tilt in opposite directions. The sectors connecting two triangles must then also bend in order to remain connected to their triangles. A ready *isometric* choice for this deformation is to bend the flat sectors into *circular conical arcs* as the boundaries of each sector squeeze together. These arcs do not in general join smoothly with their adjacent triangles, as further discussed in Sec. 2.32.4.3.

2.4 Comparing simulated deformation with model

In this section, we test whether the isometric/developable cone-triangle construction is able to predict the quantitative features of our simulated inner Lamé deformation from Sec. 2.2. Our finite-element analysis (FEA) software Abaqus uses standard methods to represent the deformed equilibrium shape as the inner boundary is gradually contracted inward. The inner boundary is allowed to buckle by moving along the cylinder (see *Methods*). For simplicity we restrict this motion to the axial direction, and allow no azimuthal motion of the boundary points. We describe the effect of this restriction in Sec. 2.5.3. In comparing this calculation to the cone-triangle construction, we must supply two free parameters: the boundary displacement Δ, as well as the wavenumber m. Thus, we record the Δ and m of the calculated deformation, and then construct the corresponding geometric solution with the same Δ and m. The first comparison we make is purely qualitative – we superpose the two solutions and observe how well they match up. Fig. 2.3 shows such a comparison, where we have rotated the geometric solution about the z-axis to obtain the best superposition. As the figure shows, one may align the two figures so that they overlay well over a significant part of the annulus, with matching zigzags at the inner boundary and matching waves at the outer boundary. Between the inner and outer boundaries, the surfaces match closely enough that the two surfaces alternately hide each other.

The qualitative resemblance seen in the figure encourages a more quantitative comparison. In particular, we propose that for a given wave number m, the shape of the sheet approaches an isometric cone-triangle structure in the limit of zero thickness. Further, approximating each cone as a circular cone sector that connects its neighboring triangles gives a useful match to the shape and energy of the sheet. Accurate comparison is hindered by the variability of the simulated wrinkles. Though regular in general, the wrinkle pattern is not strictly periodic on the annulus. To optimise the comparison, we perturb the initial flat state of the numerical sheet to promote periodicity. Specifically, we deform the initial state with a low-amplitude, smooth, periodic wrinkle with a wavelength similar to the original simulations. [2]

2.4.1 Inextensibility and bending strains

We first verify the anticipated isometry of the sheet as announced in the *Introduction*. To this end, we measure changes in lengths of the material circles at the inner ($r = 1$) and outer ($r = 1 + w$) boundaries.

---

[2] The initial wrinkle shape chosen is an eigenmode obtained from linear stability analysis performed using the FEA software.

First, we consider *radial* inextensibility. A material circle at radius r in the annulus has fixed initial arc length $L_0(r) = 2\pi r$. If this circle is displaced radially by an amount $e_r(r)$, then its horizontal projection must have length $L_{xy}(r) = 2\pi(r + e_r)$ [3]. The fractional change in the projected length L_{xy} is thus given by

$$L_{xy}/L_0 = 1 + e_r/r. \tag{2.1}$$

At the inner boundary ($r = 1$), $e_r = -\Delta$ because of the imposed boundary conditions. However, at the outer boundary ($r = 1 + w$), e_r is free to assume any value. If it's different from $-\Delta$, this implies the presence of radial stretching. In Fig. 2.4a, we plot, for a representative sample, the left side of Eq. 2.1 at both boundaries against Δ/r , as a function of changing Δ. L_{xy} here is calculated by adding up the projected lengths of the straight segments comprising the numerical boundary circles. We find that, to visible accuracy, the data points at *both* boundaries line up perfectly with the line $1 - \Delta/r$, implying that $e_r = -\Delta$ also at $r = 1 + w$. By continuity and smoothness, we conclude that $e_r(r) = \text{const.} = -\Delta$ for the entire annulus, and that the annulus is radially inextensible.

We may gauge *azimuthal* extensibility by measuring the full (not projected) change of arc length for the circle at radius r. Here we consider only the outer boundary region. As reported in Fig 2.4b there is a nonzero compression of these circles.

This compression reflects the *Elastica* bending stress of pure bending mentioned in Sec. 2.2. Specifically, bending at a scale λ produces a residual bending stress, $\sigma_{\theta\theta}^{\text{resid}} \sim -B/\lambda^2$, where B is the bending modulus. Thus, from wrinkling of wavenumber m, we expect the outer boundary to have an azimuthal bending *strain* given by:

$$\epsilon_{\theta\theta}^{\text{resid}} \sim -\frac{1}{Y}\frac{B}{\lambda^2} \sim -\frac{m^2 t^2}{(1+w)^2}, \tag{2.2}$$

where we have used $\lambda = 2\pi(1 + w)/m$ and $B/Y \sim t^2$ (t is the thickness). The strain $\epsilon_{\theta\theta}^{\text{resid}}$ is calculated for our numerical samples by directly measuring the change in azimuthal bond lengths along a material circle slightly inside $r = 1 + w$ [4], and then averaging. $\epsilon_{\theta\theta}^{\text{resid}}$ is negative as expected; moreover, it is roughly independent of Δ beyond a transient initial phase. Fig. 2.4b shows a log-log plot of $|\epsilon_{\theta\theta}^{\text{resid}}|$ for multiple samples with differing values of m, t and w. We see data collapse over the range of a decade, with the predicted slope of unity. Based on the linear fit, the estimated pre-factor for Eq. 2.2 is 0.24. We note that this is

---

[3] Here we treat the radial lines in the material as nearly horizontal, as they are for large wavenumber m.

[4] This is done to avoid possible strain originating in Gaussian curvature boundary layers at the free outer boundary of the annulus; see [27].

roughly 50 times greater than the pre-factor calculated theoretically for purely rectangular *Elastica* bending, which gives $\sigma^{\text{resid}} = -2B/\lambda^2$ [6]. Such a larger value, however, is not unexpected given the inherently two-dimensional nature of our conical *Elastica* arcs.

Figs. 2.4a and 2.4b together provide strong evidence for radial and azimuthal inextensibility of the numerical solutions. Such one-dimensional measurements of length conservation serve as a valuable proxy for testing two-dimensional isometry of the solutions, which would be far more cumbersome to measure.

2.4.2 Evolution of wrinkle amplitude

We now compare specific features of the wrinkle shape to the predictions of the cone-triangle construction. In Fig. 2.4c, we consider the amplitude of the observed wrinkles. A dimensionless way of measuring the amplitude is by determining the average slope angle α of the wrinkles at the inner and outer boundaries. Though the cone-triangle construction can be implemented for a wide range of wavenumbers m for any given Δ and w, we considered only the narrow range of m that appeared spontaneously in the unperturbed numerics, where $7 \lessapprox m \lessapprox 35$.

We define the average slope angle α to be the slope angle of the line joining the zero-crossing of the wrinkle with the adjacent maximum (illustrated in inset of Fig. 2.4a). For angle α_{in} at the inner boundary, the figure explicitly relates α_{in} to L_{xy}/L. Using Eq. 2.1, we have:

$$\cos\alpha_{\text{in}} = 1 - \Delta \equiv 1 - \tilde{\Delta}(1). \tag{2.3}$$

At the outer edge, L_{xy}/L is the ratio of the horizontal line to the arc length of the circular sector (see inset of Fig. 2.4a). For our circular cone model, it is related to the slope angle α_{out} by

$$\sin 2\alpha_{\text{out}}/(2\alpha_{\text{out}}) = L_{xy}/L \equiv 1 - \tilde{\Delta}(1+w). \tag{2.4}$$

In Fig. 2.4c, we compare these cone-triangle slope angles to the simulated ones as a function of $\tilde{\Delta}(r)$ for both inner ($r = 1$) and outer ($r = 1 + w$) boundaries. The upper red curve and data points compare α_{in}. The agreement of the data points with the curve confirms that each triangle segment tilts to preserve its length as it is drawn towards the axis. The solid black curve gives the cone-triangle prediction of Eq. 2.4 for α_{out}. The data points on and beneath the curve represent annuli of different widths w and wavenumber m, coloured by their splay: $\eta \equiv \pi(1 + w)/(mw)$. In general, our circular cone model is consistent with the prediction for narrowly-splayed wrinkles, but over-estimates the slopes for widely-splayed ones. The pictures below the graph show the annulus shape for different amounts of splay

η. They suggest the source of the over-estimated slopes: for the widely splayed example with the greatest discrepancy, the boundary curve is significantly flatter than a circular arc. Thus the simplifying assumptions of our circular-cone construction are not satisfied in this widely-splayed regime.

2.4.3 Comparing energies

Perhaps the main significance of this isometric deformation is that its energy behaves so differently from that of a generically deformed sheet. It is different in two respects. Firstly, the energy depends only on the bending modulus B, and is independent of the stretching modulus Y for given bending modulus. Secondly, the energy in this limit is qualitatively smaller than for a generic deformation with comparable curvature and thickness. Below we verify that the energy of the contracted annulus has these distinctive features.

The elastic energy is a sum of strain energy and bending energy:

$$U_{\text{elastic}} = U_{\text{strain}} + U_{\text{bend}}$$

Thus, for a strain-free isometric configuration, we have $U_{\text{elastic}} \approx U_{\text{bend}}$. For an arbitrary conical deformation extending between lengths L_{min} and L_{max} along the cone axis, the bending energy is given by:

$$U^{\text{cone}}_{\text{bend}} = \frac{B}{2} \log(\frac{L_{\text{max}}}{L_{\text{min}}}) \int ds \, \kappa^2, \tag{2.5}$$

where $\kappa(s)$ is the normal curvature of the outermost arc of the cone, parameterised by the arc length s. For a circular cone as in our model, $\kappa(s) = \text{const.} = 1/\rho_{\text{c}}$, where ρ_c is the radius of the outermost circle. Then, adding up the contributions of $2m$ cones for a wrinkled solution of wavenumber m (see SI for details), we get:

$$U^{\text{model}}_{\text{elastic}}(\Delta) = U^{\text{model}}_{\text{bend}}(\Delta) \approx B \log(\frac{L_{\text{max}}}{L_{\text{min}}}) \frac{\pi(1+w)w}{\rho_c^2(\Delta)}, \tag{2.6}$$

where the approximation is for large-m solutions. Here, the bending modulus $B = \frac{Et^3}{12(1-\nu^2)}$ (with E the Young's modulus, ν the Poisson ratio, and t the thickness) can be calculated directly from the material properties of the finite-element model. Also, in order to avoid high-curvature regions near the inner boundary, where the thin-sheet approximation $\kappa t \ll 1$ becomes questionable, we choose to compare energies for only the outer $3/4^{th}$ part of the annulus, so that $\log(\frac{L_{\text{max}}}{L_{\text{min}}}) = \log(4)$.

In Eq. (2.6) only the quantity $\rho_c(\Delta)$ is not explicitly known. Our circular cone construction (see SI) permits us to get an expression for $\rho_c(\Delta)$ in terms of the outer slope angle

α_{out}:

$$\rho_c(\Delta) \approx \frac{\pi(1+w)}{4m}\frac{1}{\alpha_{\text{out}}(\Delta)}. \tag{2.7}$$

We recall that α_{out} depends only on w and Δ, and not on m. Thus $\rho_c \sim 1/m$, and so $U^{\text{model}}_{\text{elastic}} \sim m^2$, which is the quadratic scaling with wavenumber (at fixed amplitude) expected for a bending energy.

Our primary subject of interest, however, is the scaling of $U^{\text{model}}_{\text{elastic}}$ with Δ for fixed m. Since $\alpha_{\text{out}}(\Delta) \sim \sqrt{\Delta}$ approximately (see Fig. 2.4c), we expect the squared curvature and the bending energy to scale linearly with Δ: $U^{\text{model}}_{\text{elastic}} \sim 1/\rho_c^2 \sim \Delta$. We note that this linear form is the same as for the *Elastica* energy of a rod under weak Euler buckling [28], which is expected since each transverse arc of the cone undergoes Euler buckling with this same Δ dependence.

We many compare this isometric energy with that of conventional wrinkles [6] whose height $h(r,\theta)$ has the separable form $h = f(r)\sin(m\theta)$. As discussed in the SI, radial wrinkles of this form have substantial strain ϵ_c of order of $\epsilon_c \simeq \Delta/m^2$, much larger than the bending strain of Eq. 2.2, viz. $\simeq\ m^2t^2$. Accordingly, for fixed Δ and m the conventional strain ϵ_c and its associated elastic energy are much larger than their bending counterparts as $t \to 0$.

In Fig. 2.5, we plot three energy curves for a typical sample. These curves compare the simulated energy for a typical example, $U^{\text{sim}}_{\text{elastic}}(\Delta)$ (lower curve), with two theoretical estimates: $U^{\text{model}}_{\text{elastic}}(\Delta)$ (upper curve; see Eq. 2.6) calculated from our cone-triangle model, and $U^{\text{sim}}_{\langle\kappa^2\rangle}(\Delta)$ (middle curve) calculated indirectly from the simulated solution through measurement of the mean squared curvature at the outer boundary: $\langle\kappa^2\rangle_{\text{out}} \equiv \frac{1}{2\pi(1+w)}\int ds\ \kappa^2$, and by using Eq. 2.5. The three curves are similar, differing by a roughly constant factor of order unity. Notably, the full simulated energy including any strain energy, is smaller than the model bending energies. This discrepancy is natural for the circular cone model, since this circular anatz does not minimize the bending energy. The assumed uniform, circular curvature does not minimize the energy of the cone shape needed in order to bridge between the adjacent triangles. We expect that the system chooses a curvature profile $\kappa(s)$ that minimizes this energy. Thus, as expected, the use of the measured $\kappa(s)$ improves the agreement with the measured energy greatly. We have not settled the source of the remaining discrepancy, discussed in the SI. Measurements of local curvature such as $\kappa(s)$ on a finite-element surface is prone to uncertainties. Moreover, we cannot rule out the possibility that the directors fail to converge to a point; this failure would mean a loss of isostaticity and would be expected to decrease as thickness decreases.

We conclude that the elastic energy of deformation for the wrinkles encountered in this study is strongly consistent with our claim of an isometric conical deformation. Furthermore, the explicit circular-cone-triangle construction gives a workable quantitative estimate of the full elastic energy, provided we supply the observed wrinkle wavenumber m. This approximation is least accurate when the splay parameter η is large.

2.5 Discussion

2.5.1 A developable wrinkling morphology

As shown above, our variant of the Lamé radial contraction system is qualitatively altered by removing the outer tension from that system. The mechanics in our system is governed instead by the constraints of isometric deformation, dictating a developable surface in the limit of zero thickness. While developability has been hypothesised and used as tool to study buckling in several contexts [5, 8, 12, 29, 30], in our favourable case, we have been able to account for all the details of the structure with a simple periodic cone-triangle *Ansatz*.

To the best of our knowledge, such reconstruction of a wrinkled configuration through fundamental developable building blocks is novel in the field of thin sheet elasticity. That an *a priori* complicated wrinkled surface can be broken down into such a two-part *macroscopic* unit cell is indicative of the strong geometric simplifications brought about by developability and Gauss' *Theorema Egregium.* Furthermore, unlike previously-known faceted structures – which are composed of only flat facets [31–33] – faceted wrinkling has both flat triangles and curved cones. This cone-triangle decomposition also provides an instructive example of a buckled shape in a radially symmetric system that does not have the conventional separable form – i.e. the buckling displacement is not a product of a radial factor and azimuthal factor.

The developability of the faceted wrinkling structure makes it fundamentally geometric, so that it can be created easily on a computer. This provides a way to programmatically construct *smooth* radially wrinkled patterns in materials using intrinsically flat components, much in the spirit of origami and other designed materials [4].

In fact, a well-known real world example of such programmed radial wrinkling is the Elizabethan ruff collar. One way of making a ruff is exactly using the inner Lamé boundary conditions: we take a cloth annulus, and manually make pleats in it such that the inner boundary of the annulus lives on a contracted radius. Figs. 2.1e and 2.1d show, respectively, a ruff collar and its reconstruction using our circular-cone-triangle model; the visual similarity between the two is striking. The conical outer solution seems to capture the ruff wrinkles, in particular their radial straightness and their shape at the outer boundary.

We note that accounting for the wrinkles of Fig. 2.1c is not equivalent to finding a ground-state configuration consistent with the imposed boundary condition. Our deformation was performed quasistatically, and the wrinkles appeared continuously without abrupt jumps. Thus the system followed a single energy minimum as it deformed. This observed deformation may well have significantly higher energy than the ground state has.

2.5.2 Nature of the thin-sheet limit

The wrinkles investigated here closely approximate the isometric cone-triangle structure, as shown above. This leads us to ask what is the limiting structure as the thickness approaches zero. This limit has two aspects. On the one hand, we found that the wrinkle wavelength decreases with decreasing thickness. On the other hand, our studies identified a particular cone-triangular structure, definable independently of wrinkle wavelength, which closely approximated the shape and energy of the numerical sheet. Since this structure is by construction free of strain, we expected the numerical sheet to have little strain. Our measurements of elastic energy in Fig. 2.5 confirmed this; no energy beyond the expected bending energy was observed even up to our largest thickness of 2.7×10^{-2}. The most significant strains appeared near the tips of the zigzags, as one expects near the vertex of a cone. These findings suggest that the approach to this isometric structure with decreasing thickness occurs independently of wavelength. Establishing this structure lays the groundwork for understanding the selection of wavelength. A separate paper by one of us, under review [24], addresses this wavelength selection question.

2.5.3 Approximations and limitations

Circular cone *Ansatz*

The key modelling assumption used in this paper is the circular *Ansatz* for the bent cones. As we have shown, this *Ansatz* serves as a serviceable approximation to the true energy-minimising *Elastica* solution, while being simple enough to allow for explicit calculation of several key observables, namely, the slope α_{out} and the energy U_{elastic}. Sec. 2.4 shows that this approximation is accurate only for relatively narrow cones (small η) and large w. This can be partially explained as follows. We expect the circular *Ansatz* to hold true only for *weak* Euler buckling. "Weak" here means that the angular squeezing of the cones and the resultant slope, are both small. In the SI, we show that this squeezing experienced by a conical sector during deformation increases sharply with decreasing w, such that for our narrowest annuli, it can be as high as 20% for our maximum Δ. At such large values, one no longer expects the weak Euler regime to be valid, and the resultant shape manifests its non-linearity through the flattening apparent in Fig. 2.4c. We note, however, that even at such large contractions, both the circular *Ansatz* and the numerical simulations give a linear energy profile, although their slopes are no longer close.

Inner boundary approximation

Despite this strong resemblance between the simulated wrinkles and the cone-triangle structure, the match cannot be exact. Our construction of the cone-triangle shape in Sec 2.3 required that the inner boundary be a polygon. It is only a good approximation to the simulated circular annulus when the wavelength (*i.e.* $2\pi/m$) is sufficiently small. In particular it must be small in relation to the width w if the triangles are to resemble those of Fig. 2.1. Details are provided in the SI, Sec. 2.7.3. The inexactness of the triangle construction at the inner surface makes it clear that the construction is not a realistic representation of a circular annulus contracted onto a cylinder for *arbitrary* wavenumber m. We demonstrated the isometric shape for only a limited range of geometries; both the displacement Δ and the width w were confined to moderate ranges. For these moderate conditions the system appears to choose wavelengths fine enough that the inaccuracies of the cone-triangle construction are not important. For more extreme ranges, we expect that the cone-triangle picture shown here will need modification and that the $t \to 0$ limit will be more subtle. In particular, the locally stable isometric structure observed here may give way to previously-identified divergently fine wrinkling[6].

Finding the conditions in which the cone-triangle wrinkles occur is a fruitful subject for future work.

Lateral constraint boundary condition

As noted in *Methods*, we prohibit any lateral movement of the nodes on the inner boundary, in order to stabilise the faceted wrinkled regime against folding instabilities. However, even if we do allow lateral movement, we see the same faceted wrinkling at early simulation times, before azimuthal movement of the boundary eventually leads to folding. That is, the, excess material concentrates at a single sector along the circumference. Our observations suggest that faceting can be seen for initial buckling, even in the absence of lateral constraints. But our evidence is still only suggestive and needs to be confirmed through physical experiments.

2.5.4 Application

The deformation geometry treated here amounts to a strategy for avoiding the typical fate of deformed sheets. Such sheets adopt structures that require significant elastic energy beyond the needed bending energy. Often these structures produce uncontrolled disorder, *e.g.* as seen in a crumpled sheet. By contrast, the radial contraction used here guides the sheet into a locally low-energy channel resulting in only bending energy. This low-energy state is moreover attainable by continuous deformation from a flat reference state. Since these deformations lack the additional deformation costs of competing structures, they are intrinsically (locally) stable. They provide a general means to fold and compact a sheet continuously and reversibly with minimal external guidance. We note that the curved inner boundary appears important in stabilising this structure; straight boundaries with no radial contraction [14] do not produce analogous regular wrinkling.

These guiding channels should appear more generally than in the simple circular geometry studied here. The same principles control other inwardly curved boundaries, and other directions of contraction, e.g. onto a constraining cone instead of a cylinder.

Conclusion

While the emergence of developability in wrinkled systems has been studied intensively over the past decade, the simplicity and symmetry of the inner Lamé geometry makes it a particularly clean realisation of such a phenomenon. This faceted morphology is qualitatively different from previously known forms of two-dimensional wrinkling. Significantly, it creates sharply dictated, strongly distorted features without stretching and without a separable radial/azimuthal shape. Moreover, it has many variants to be explored, with real world applications. Finally, this work sets the stage to explain the selection of the wavenumber m. We address this in a separate work [24].

2.6 Methods

To investigate the wrinkling morphology of the inner Lamé system, we used the commercial finite-element (FE) solver Abaqus 2018 (SIMULIA, Dassault Systèmes). Using both implicit and explicit dynamic methods[5] in a quasi-static regime, we performed simulations of the inner Lamé system using its defining boundary conditions: radial displacement $e_r(r=1) = -\Delta$ at the inner boundary, and the outer boundary at $r = 1 + w$ free. The maximum value of Δ applied was $\Delta_{\max} = 0.267$. To account for the possibility of high strains, the sheet was initially modelled as a Neo-Hookean hyperelastic material with coefficients equivalent to the linear moduli: Young's modulus, $E = 0.907125$ MPa, and Poisson ratio, $\nu = 0.475$

---

[5] 'Dynamic' means through time integration of the equations of motion. 'Implicit' (using a modified Newton-Raphson method) and 'explicit' refer to the method of integration.

(c.f. Eq. 2.6), corresponding to a rubber-like material. To verify that results are independent of the material model, we also re-performed several simulations with a linear material model with these same moduli. Further details on our FEA methods are given in the SI.

To test the validity of our results over a range of parameters, we kept the inner radius fixed and varied the other two parameters – width w and thickness t – over the range of a decade. The width w of the annulus was varied between $w = 0.33$ (very narrow) to $w = 1.67$ (moderately wide) – a factor of almost 10. The thickness t was varied between $t = 2.67 \times 10^{-3}$ (thick) to $t = 1.33 \times 10^{-4}$ (very thin), a factor of 20. We performed consistency checks to ensure that the final morphology was independent of the choice of any simulation parameters. For data extraction, we used the software package Abaqus2Matlab [34].

We used two principal deformation protocols to ensure that the wrinkles we observed were characteristic of the quasi-static limit. Our baseline protocol was done using explicit dynamics, in which the finite elements are accelerated with a constant damping factor. The other deformation protocol used an implicit scheme for integrating the forces, with the damping factor automatically selected by the software to favour quasi-static behaviour. In both cases, to avoid gross kinetic effects, we increased Δ from 0 to $\Delta_{\max}$ at a rate slow enough such that the kinetic energy of the system always remained $\lessapprox 5\%$ of the elastic energy. This is standard procedure for quasi-static analyses in finite-element simulations (see SI for details).

Boundary conditions

The specifics of the wrinkling morphology depend on how the contracted boundary is constrained. For example, the clamped boundary studied by Mora and Boudaoud [11] leads to a highly compressed boundary layer whose relation to the sheet is difficult to discern. The other extreme is to allow each point on the boundary circle to lie anywhere on the confining cylinder; such boundaries lead to wrinkling only in a transient regime, leading ultimately to collapse into a fold. Here we study an intermediate constraint in which points on the bounding circle may move only axially (i.e. vertically) on the bounding cylinder; azimuthal (θ) motion is not allowed. Doing so automatically prohibits folding (since this requires lateral motion), but without interfering with the wrinkling.

Acknowledgements

The authors would like to thank Benny Davidovitch, Dominic Vella and Enrique Cerda for many insightful discussions, and Nhung Nguyen and George Papazafeiropoulos for help with numerical analysis. This work was partially funded by the National Science Foundation (NSF)-Materials Research Science and Engineering Center (MRSEC) grants DMR-1420709 and DMR-2011854.

2.7 Supplementary Information

2.7.1 SI: Construction of circular conical sections

In the main text, we describe how we divide the flat annulus into two regions – an inner region composed of isosceles triangles, and an outer region composed of arc sectors. The main text describes how the inner triangles can isometrically deform under an inner displacement (or contraction) of length Δ by tilting about the normal to the inner boundary – this gives an inner 'buckled' solution. Here, we describe how to construct the outer solution whereby the arc sectors isometrically bend into sections of right-circular cones. In other words, each arc bends into a circular profile.

The requisite variables for our geometric construction are described in Fig. 2.6. In the flat state, each arc sector, lying between two adjacent flat triangles, subtends an angle ϕ_f at the common vertex of these two triangles. If the edges of the triangles have length R_f, then the length of the largest arc is $L = R_f \phi_f$. On tilting, the edges of these same triangles approach each other, so that they subtend a reduced angle ϕ_t (see SI Fig. 2.7a). This reduction in angle ($\Delta\phi = \phi_t - \phi_f \leq 0$) constitutes the effective compressive strain $\epsilon_{\text{cone}} = \Delta\phi/\phi_f$ for the arc sector. SI Fig. 2.7a shows the evolution of ϵ_{cone} with boundary contraction Δ. We see clearly that narrower sheets feel a greater ϵ_{cone} for the same Δ.

The excess material can be accommodated by bending the sector into a cone. The exact shape of this cone can be determined by solving the *Elastica* equation with the appropriate boundary conditions. However, for simplicity, in this paper we choose to approximate the exact shape by a circular cone. The aim then is to find the circular cone that fits in between the two adjacent triangles while exactly accommodating the excess angle $\Delta\phi$. Fig. 2.6b shows all the variables needed for this operation. The isometrically bent conical section has to fit inside the triangle $\triangle AOB$ (drawn in teal) defined by the apex 0 and the tilted edges OA and OB (see also Fig. 2.3 in main text). The conical section itself is drawn in bold black. Let the circular cone have angular extent ϕ_c, and let its maximum radius be ρ_c, centred at point C. Then the conical shape can be determined from the following set of geometric constraints.

The first constraint is that of inextensibility, i.e. length conservation. This gives us:

$$L = \rho_c \phi_c = R_f \phi_f. \tag{2.8}$$

The second constraint involves specifying the end-to-end distance L_1 between points A and B. Thus, using the blue triangle $\triangle AOB$ and the grey triangle $\triangle ACB$ in Fig. 2.6b, we have:

$$L_1 = 2\rho_c \sin(\phi_c/2) = 2R_f \sin(\phi_t/2). \tag{2.9}$$

Eqns. (2.8) and (2.9) constitute a set of simultaneous equations for the cone variables ρ_c and ϕ_c, since R_f and ϕ_f are fixed by the flat geometry, while ϕ_t is set by the tilt of the neighbouring angles. Finally, using basic trigonometry, we have for the cone's apex angle:

$$\sin\beta = \rho_c/R_f. \tag{2.10}$$

In sum, we have three independent equations for three unknowns: ϕ_c, ρ_c and β (all positive-definite), which fully specify the cone in space (including the centre C). SI Fig. 2.7b shows a representative solution of such a constructed cone. SI Fig. 2.7c shows the evolution of this construction with increasing Δ.

2.7.2 SI: Correcting for scalloped arc sectors

The flat arc sectors as defined above – circular arcs with their origin at the inner boundary – lead to the creation of a flat shape that is in fact a *scalloped* annulus, whose outer circumference $2mR_f\phi_f$ is greater than the expected $2\pi(1+w)$.

We can correct for this length discrepancy when constructing the bent cones, by changing $R_f \to \chi R_f$ in Eq. (2.8) where $\chi = \frac{\pi(1+w)}{mR_f\phi_f} \leq 1$. Eq. (2.9) remains unchanged since it specifies the end-to-end-distance, which is set by the neighbouring tilted triangles. We note that this factor χ is smallest for samples with small w and m (wide splay η), and becomes ≈ 1 for large w and m (narrow splay).

2.7.3 SI: Limits of the cone-triangle construction

To the best of our knowledge, the above conical construction works as long as the initial (flat) angle $\phi_f < \pi$, i.e. as long as the edges of two adjacent triangles define a triangle. The value of ϕ_f depends on the width w and the wavenumber m, and increases as m decreases. This defines a minimum wavenumber $m^{\text{cone}}_{\text{min}}(w)$ below which a conical solution is invalid. For a sufficiently wide annulus, we find that $m^{\text{cone}}_{\text{min}} = 2$, which is the minimum possible value for *any* wrinkled solution. However, for very narrow annuli, this value goes up. Thus, for $w = 0.2$, we find $m^{\text{cone}}_{\text{min}} = 4$. Fig. 2.8 shows two such contrasting geometries. $m^{\text{cone}}_{\text{min}}(w)$ defines a geometric limit beyond which we expect our cone-triangle model to fail. However, the main text shows that we already see significant deviations from our model for Abaqus solutions with wavenumber m significantly higher than $m^{\text{cone}}_{\text{min}}(w)$.

2.7.4 SI: Calculating the conical strain $\epsilon_{\text{cone}}(\Delta)$

Fig. 2.7a shows the evolution of the conical strain ϵ_{cone} with contraction Δ. The observations (plotted with dots) show that $\epsilon_{\text{cone}}(\Delta)$ is linear, with the slope depending significantly on the width w of the sheet, but independent of the wavenumber m. To understand this behaviour, we analytically derive an expression for $\epsilon_{\text{cone}}(\Delta) = (\phi_t - \phi_f)/\phi_f$.

Since ϕ_f is fixed, to find ϵ_{cone}, we only need to calculate $\phi_t(\Delta)$. The angle $\phi_t(\Delta)$ can be calculated given any one of the inner triangles, the flat arc angle ϕ_f, and the tilt angle α. The geometric problem is defined in Fig. 2.9. Here, ϕ_t is the angle between the rotated vector $\overrightarrow{QR'}$ and the vertical blue plane defined by $\overrightarrow{RZ}$. Also, w is the annular width, and $h = \pi/m$. Then our steps are as follows:

1. Find the 3-vector $\overrightarrow{OR'} = \mathbb{R}_{-\alpha} \cdot \overrightarrow{OR}$, where $\mathbb{R}_\alpha$ is the 2x2 rotation matrix of angle α about the y-axis (viz. $\overrightarrow{OQ}$).
2. Then $\overrightarrow{R'Q} = \overrightarrow{OQ} - \overrightarrow{OR'} = (-h/2\cos\alpha, w, h/2\sin\alpha)$.
3. We only needs its orthogonal projection on to the x-y plane: the 2-vector $\overrightarrow{R'Q_\perp} = (-h/2\cos\alpha, w)$.
4. We need the vector angle between this and the vertical blue plane defined by $\overrightarrow{RZ}$. Here, $\overrightarrow{RZ} = \mathbb{R}_{-\phi_f/2} \cdot \overrightarrow{RQ}$, where $\overrightarrow{RQ} = (-h/2, w)$.

Finally, we have $\phi_t = 2\text{VectorAngle}[\overrightarrow{R'Q_\perp}, \overrightarrow{RZ}]$. The final expression is complex and composed of trigonometric functions. But using $\cos\alpha = 1 - \Delta$ (recall that the inner radius $= 1$), and expanding to linear order in Δ, we have:

$$\Delta\phi \equiv \phi_t - \phi_f \approx -\frac{h/w}{(h/2w)^2 + 1}\Delta + \ldots, \tag{2.11}$$

where $h/w = \frac{\pi}{mw} \ll 1$ for most of our samples. Finally, we also have $\phi_f \approx \frac{\pi(1+w)}{mw}$, where

$1+w$ is the outer radius. Therefore, we get for the dimensionless conical contraction:

$$\epsilon_{\text{cone}} \equiv \frac{\Delta\phi}{\phi_f} \approx \frac{h}{w\phi_f}\Delta \approx -\frac{1}{1+w}\Delta. \tag{2.12}$$

The prediction of Eq. 2.12 is plotted alongside measurements in the inset of SI Fig. 2.7a. The two are fully consistent. This explains why wider cones should feel less contraction for a given Δ.

2.7.5 SI: Calculating bending energy for a cone

In this section, we continue with the variables introduced in section SI-I. A right-circular cone is made up of a series of circles whose radii ρ increase linearly with distance (say, z) along the cone axis, measured from the cone tip. For a cone of axial length L_c (see SI Fig. 2.7a) and maximum radius ρ_c, we thus have: $\rho(z) = \frac{\rho_c}{L_c} z$. We can also write $\frac{\rho_c}{L_c} = \tan\beta$, where β is the cone's vertex angle.

Now, an infinitesimally wide circular band of radius ρ, angular extent ϕ_c, and width $\frac{dz}{\cos\beta}$, has bending energy $= \frac{B}{2}\frac{1}{\rho^2} \times (\phi_c\rho) \times \frac{dz}{\cos\beta}$, where B is the bending modulus. Integrating over an entire conical sector, we get:

$$U_{\text{bend}}^{\text{cone}} = \frac{B}{2}\frac{\phi_c}{\cos\beta}\int_0^{L_c} dz\, \frac{1}{\rho(z)} \tag{2.13}$$

$$= \frac{B}{2}\phi_c \frac{1}{\cos\beta\tan\beta}\int_0^{L_c}\frac{dz}{z} \tag{2.14}$$

Any physical cone must have a *finite* bending energy, and thus must depart from the conical shape near $z = 0$. Thus, the conical shape can only be realistic beyond a minimum axial distance L_{core}. For this outer region, the energy becomes:

$$U_{\text{bend}}^{\text{cone}} = \frac{B}{2}\frac{\phi_c}{\sin\beta}\log(\frac{L_c}{L_{\text{core}}}), \tag{2.15}$$

where $\beta = \tan^{-1}\frac{\rho_c}{L_c}$. For small angle β (i.e. large Δ), Eq. (2.15) can be simplified to:

$$U_{\text{bend}}^{\text{cone}} \approx \frac{B}{2}\phi_c\frac{L_c}{\rho_c}\log(\frac{L_c}{L_{\text{core}}}), \tag{2.16}$$

Here, ϕ_c, ρ_c and L_c are all functions of the contraction Δ. But ϕ_c and ρ_c are related through the constraint: $\phi_c\rho_c = L = \frac{\pi(1+w)}{m}$ (see Eq. 2.8), and $L_c \approx w$ (the width of the annulus), so $U_{\text{bend}}^{\text{cone}}$ can be reduced to a function of the single variable ρ_c. For the entire annulus, we need to multiply this by the number of cones $2m$. Thus, we get:

$$U_{\text{bend}}^{\text{theory}} \approx B\frac{\pi(1+w)w}{\rho_c^2}\log(\frac{w}{L_{\text{core}}}), \tag{2.17}$$

More generally, for a cone extending between axial limits $L_{\min}$ and $L_{\max}$, we have:

$$U_{\text{bend}}^{\text{theory}}(\Delta) \approx B\frac{\pi(1+w)w}{\rho_c^2(\Delta)}\log(\frac{L_{\max}}{L_{\min}}), \tag{2.18}$$

This is the expression given in the main text.

While Eqs. (2.17) and (2.18) seem independent of m, it is not so. Eq. (2.7) in the main text shows that $\rho_c \sim (1+w)/m \implies U_{\text{bend}}^{\text{theory}} \sim m^2$, as expected of a bending energy. We note that this $\rho_c \sim 1/m$ scaling could have been predicted in another way. In the limit of maximum contraction ($\Delta \to 1$), the point C approaches the xy-plane, and so the diameters of the $2m$ circles must approximately equal the reduced projected outer perimeter: $2\pi(1+w-\Delta) \to 2\pi w$. This gives us: $4m\rho_c \to 2\pi w \implies \rho_c \to \frac{\pi w}{2m}$ (the dotted line in the inset of SI Fig. 2.7c). Indeed, even if C is off the x-y plane (e.g. for smaller Δ), the diameters of the $2m$ circles must still equal the reduced perimeter $2\pi(1+w-\Delta)$ up to some factor. Thus, we have the scaling relation $\rho_c \sim 1/m$ as expected.

Finally, we note that the data presented in the paper represents the full expression 2.15, without any approximation.

2.7.6 SI: Comparison with separable, sinusoidal wrinkling

The cone-triangle shape described in the main text sharply reduces the elastic strain and energy relative to conventional wrinkling with height profile $h^c(r,\theta)$ *e.g.* of the form [6]

$$h^c(r,\theta) = f(r)\cos(m\theta) \tag{2.19}$$

as we now illustrate.

In the far-from-threshold regime, this h^c profile must relax the azimuthal stress $\epsilon_{\theta\theta}$ arising from the inward displacement $u_r = -\Delta$. In general this azimuthal stress has the form [20]:

$$\epsilon_{\theta\theta} = \frac{u_r}{r} + \frac{1}{r}\partial_\theta u_\theta + \frac{1}{2r^2}(\partial_\theta h^c)^2 \tag{2.20}$$

For purposes of comparison we may evaluate this ϵ at a zero of $h^c(r,\theta)$ *e.g.* $m\theta = \pi/2$. There by symmetry the azimuthal displacement $u_\theta = 0$ and $\partial_\theta u_\theta = 0$. Thus the second term in Eq. 2.20 vanishes. In the last term $\partial_\theta h^c = \pm m f(r)$. We use this expression to estimate $\epsilon_{\theta\theta}$. Choosing $h^c(r, \theta)$ to make $\epsilon_{\theta\theta}$ vanish implies

$$\Delta \simeq \frac{1}{2r} m^2 f(r)^2 \tag{2.21}$$

So that $f(r) \simeq \frac{1}{m}\sqrt{2r\Delta}$

This non-constant $f(r)$ entails a radial strain ϵ_{rr} given by [20]

$$\epsilon_{rr} = \partial_r u_r + \frac{1}{2}(\partial_r h)^2 \tag{2.22}$$

Here u_r is constant as noted above and $\partial_r h \simeq \partial_r f(r) \simeq \frac{1}{m}\frac{1}{2}\sqrt{2\Delta/r}$, giving an estimated conventional wrinkle strain ϵ^c_{rr} of

$$\epsilon^c_{rr} \simeq \frac{1}{4} m^{-2}(\Delta/r) \tag{2.23}$$

This radial strain of conventional wrinkling is to be compared to the bending strain ϵ^B in the cone-triangle model. This strain arises from the bending stress $\sigma^B_{\theta\theta}$ [6]

$$|\sigma^B_{\theta\theta}| \simeq 2B(m/2\pi r)^2, \tag{2.24}$$

where bending modulus B is related to the thickness t, the poisson ratio ν and the bulk Young's modulus E by [35] Sec.12

$$B = Et\frac{t^2}{12(1-\nu^2)}. \tag{2.25}$$

Using $\epsilon = (Et)\sigma$, then Eq. 2.24 yields

$$\epsilon^B_{\theta\theta} \simeq 2\frac{t^2}{12(1-\nu^2)}(m/2\pi r)^2 \tag{2.26}$$

For the annuli simulated above the conventional wrinkles have much greater elastic strain than the bending strain we report: their ratio is given by

$$\frac{\epsilon^c}{\epsilon^B} \simeq m^{-4}(r\Delta/t^2)\ \big(6(1-\nu^2)\pi^2\big) \tag{2.27}$$

Evidently for fixed m the ratio diverges as $t \to 0$. For the specific annulus used for Fig 5 with $r = 1$, $\Delta = 0.2$, $\epsilon^c/\epsilon^B \simeq 50$. By these estimates the sinusoidal wrinkling carries substantially larger strain and thence elastic energy relative to the isometric wrinkling we report.

2.7.7 SI: departures from conical shape

Here we gauge the impact of the stretched zigzag vertices on the total energy by examining how the elastic energy varies with distance $r-1$ from the inner rim. Fig. 2.10a shows this energy for the right-most data points of Fig. 2.5. The red simulation point (lower curve) in Fig. 2.5 is found by summing the energies in each azimuthal ring of finite elements over the range of r indicated by the hashed region. The simulated ring energies for selected r are shown as black rectangles.

The corresponding cone-triangle energy, *i.e.* the right-most point on the (yellow) middle curve in Fig. 2.5, is found using the cone ring energy plotted as a solid curve, using Eq. 2.5. This equation implies a ring energy varying as $1/(r-1)$. Since the yellow point is found by matching the simulated curvature at the outer boundary, the cone model gives a ring energy that matches the simulated ring energy there, as Fig. 2.10a shows.

By comparing the simulated ring energies with the cone model, we can gain insight into the difference in energies seen in Fig. 2.5. The inner simulation point shows the expected large discrepancy with the model, which unrealistically diverges at the inner boundary. The middle simulation point is at the inner boundary of the region treated in Fig. 2.5. This ring energy is 40 percent smaller than the cone model prediction. This difference is consistent with the 15 percent differences between the energies of Fig. 2.5. Any cone that would cure this discrepancy would have to extrapolate to a vertex beyond the inner boundary.

The azimuthal strain profile shown in Fig. 2.10b also shows departures from the model. The plot shows the azimuthal dependence of the azimuthal strain $\epsilon_{\theta\theta}$ for a radial position r equidistant between the inner and outer boundaries.. The plotted strain is maximal at peaks and troughs of the wrinkles. Though the averaged strains,are consistent with bending strains, as discussed in Sec. 2.42.4.1, there are strong oscillations adjacent to these peaks and troughs with a period of two finite elements. This suggests that our simulations have limited reliability for predicting these weak strains near the peaks or troughs. Away from the peaks and troughs the strains vary smoothly. Of special interest is the point where the model cone and its adjacent triangle would meet. These points, marked by dashed lines show no sign of discontinuity.

These detailed features of Fig. 2.10 show shortcomings of the cone-triangle model. However they underscore the relevance of this model for understanding this form of buckling.

2.7.8 SI: Finite-element method (FEM) simulation details

For our simulations, we used the commercial finite-element software Abaqus 2018 (Simulia, Dassault-Systèmes, Providence, RI). This section describes the different steps for generating a typical simulation of our inner Lamé system, in the order typical of a finite-element software.

The assembly consisted of only a single annulus, with inner radius fixed and taken to be unity, and with varying width w and thickness t in order to test our system over a wide range of system parameters. For width, we used values $w = 0.20, 0.33, 0.67, 1.0, 1.67$ (a factor of almost 10, ranging from very narrow to moderately wide), and for thickness, we used values $t = 2.67 \times 10^{-3}, 1.33 \times 10^{-3}, 6.67 \times 10^{-4}, 2.67 \times 10^{-4}, 1.33 \times 10^{-4}$ (a factor of 20, ranging from moderately thick to very thin). While these thickness values vary over a decade, the values still fall well within the thin sheet limit. The annular part was made of 2d shell quad (S4R) elements [36]. This choice was made mainly to optimise speed, since we used a fine enough mesh to ensure that doubling the linear mesh size change the energy by a negligible amount ($\lessapprox 1-2\%$). For comparison, the coarsest mesh we used was for the $w = 1.67$ annulus, with 60 elements across the radius and 1400 elements across a circle, giving a maximum linear size for an element ≈ 0.01. For consistency checks however, we also ran some simulations with annuli made of 3d volume cubic (C3D8R) elements [36], which gave the same morphology (with the same wavenumber), but which much longer running times.

When discussing the material properties, for concreteness, we will use SI units (and thus take the inner radius to be 1 m). For the material properties, we mostly used a standard neo-Hookean hyperelastic model [36] with coefficients $\mathrm{C}_{10} = 1.5375 \times 10^5$ Pa, $\mathrm{D}_1 = 3.2520 \times 10^{-7}$ Pa^{-1}. These coefficients are related to the more well-known linear elasticity moduli by the relations: $C_{10} = \mathrm{G}/2$ (where G is the shear modulus), and $\mathrm{D}_1 = 2/\mathrm{K}$ (where K is the material bulk modulus). The corresponding Poisson ratio is given by $\nu = \frac{3/(C_{10}D_1)-2}{6/(C_{10}D_1)+2} = 0.475$. The Young's modulus can be obtained from either of the relations: $E = 2G(1+\nu)$, or $E = 3K(1-2\nu)$; we obtain $E = 907,377$ Pa ≈ 0.9 MPa (corresponding to a rubber-like material). As a test, we also performed several simulations with a linear material model with these values of E and ν.

The elastic modulus can be used, along with the material density ρ and the average linear mesh size l_e, to determine the average integration time scale (i.e. the 'stable time increment') in the simulation, as follows. The elastic bulk modulus K and the density ρ determine the speed of sound in the material, $c_s = \sqrt{K/\rho}$ [6]. The stable time increment in the simulation is on the scale of the time required for elastic information to traverse an average mesh element: $\Delta t \sim l_e/c_s$. For our values of $K \sim 10^5$ Pa, $\rho = 10^3$ Kg/m^3 and $l_e \sim 10^{-2}$ m, we get $\Delta t \sim 10^{-3}$ s. This in turn determines the dimensionless number of iterations n_{iter} performed by the solver in a simulation running over time period T: $n_{\text{iter}} = T/\Delta t$. Below, we discuss the typical values of T used in our simulations, and how increasing T allows us to reach a quasi-static limit in dynamic integration methods (i.e. where kinetic energy is present but negligible compare to elastic energy).

For the radial displacement loading at the inner boundary, we applied velocity and displacement boundary conditions (BCs) interchangeably. Typically, we applied velocity BCs with a linear amplitude profile, and displacement BCs with a smooth-step profile [36], in order to assure a smooth (i.e. zero velocity) pull at the beginning. These were applied so that the maximum displacement amplitude $\Delta_{\text{max}} = 0.267$ is attained within a time period T (defined in the same units as the Δt given above). The value of T was chosen to be large enough to ensure small kinetic energy and give a T-independent configuration, as defined below. Typically, we used $T = 20$ for the thicker sheets, and $T = 80$ for the thinnest sheets.

For the simulation protocol, we employed both 'dynamic explicit' and 'dynamic implicit' [36] integration schemes in the quasi-static limit (as compared to a fully 'static' energy minimisation scheme). The word 'dynamic' refers to the presence of inertia, while 'explicit' and 'implicit' refer to the solution scheme. 'Explicit' means explicit time-integration of Newton's second law, while 'implicit' refers to implicit integration (viz. through iterative root-finding) of Newton's law, using a modified Newton-Raphson method. The mixture of these two methods was done partly as a consistency check, partly for convenience, and partly by necessity. While the implicit method in the quasi-static limit was faster for most jobs, the explicit solver was indispensable for the thinnest samples, where the static solver ran into convergence problems. Ensuring the quasi-static limit is also easier for 'dynamic implicit' than for 'dynamic explicit'. In dynamic implicit, the quasi-static option is in-built, but for dynamic explicit, it has to be ensured manually by applying the loading slowly enough so that further slowing has no effect on the final shape and energy.

For this, we need to look at the available energy modes. The energy balance equation in Abaqus [36] is given by (ignoring possible terms coming from viscosity, friction, heat, contact

---

[6] Alternately, one can use the Young's modulus E instead of the bulk modulus K in the definition of c_s. But this does not qualitatively alter our argument above.

and constraint penalties, etc.), is:

$$E_I + E_{KE} - E_W = 0 \tag{2.28}$$

where E_I is the internal energy, E_{KE} is the kinetic energy, and E_W is the work done by externally applied loads. For us, the internal energy is just the elastic energy (by design, there are no other energy modes). Thus, for quasi-static loading, one generally requires the kinetic energy (E_{KE}) to be $< 10\%$ of the elastic energy (E_I). In practice, we kept the ratio to $\lessapprox 5\%$. Since the elastic energy is thickness-dependent (always increasing with increasing thickness), thinner sheets required slower applications of the loading. E.g., for the thinnest samples ($t = 1.33 \times 10^{-4}$), this involved applying the contraction Δ over a time period $T = 80 - 120$, viz. using $n_{\text{iter}} \sim 10^5$ solver iterations. As a result, the slowest simulations, for the thinnest and widest sheets, lasted ≈ 150 core-hours; the average simulation however, lasted between ≈ 30 core-hours. For reference, the validation case (described blow) of folding a flat sheet into a cylinder, albeit with a much coarser mesh, was accomplished using ≈ 0.2 core-hours.

For data extraction, we used field output for the displacement variables, and history output for the energy [36]. For the elastic energy, we used the "ALLIE" (internal energy) variable [36], equivalent to the E_I variable in Eq. 2.28. Since the simulations are done using a dynamic time-integration scheme with inertia, there is an inherent noise in the energy values arising from imprecision in finding the exact energy minimum (viz. due to inertial oscillations). We cannot estimate this noise precisely, but a rule-of-thumb estimate is $\lessapprox 5\%$, i.e. of the same order of magnitude as the ratio E_{KE}/E_I. However, in reality, it might well be less. Significantly, this noise cannot account for the discrepancy between energy measurements and model predictions in Fig. of the main text. Finally, post-processing was done using Abaqus2Matlab [34].

2.7.9 SI: Testing the numerics for known cases

We used the above procedures (albeit with a static energy minimisation scheme) to calculate an analytically solvable case, to verify that the shape and energy agreed with the known results. The example was a rectangular sheet of width $w = 1$, length $L = 2\pi$, and thickness $t = 1 \times 10^{-3}$, in which we prescribed boundary conditions on position and orientation of the short edges to make them curve up and in, to form a circular cylinder of unit radius.

We verified the circularity of the cross-section by projecting onto the plane and measuring the distance from the centre. We found that no point differed in its axial distance by more than .001%. The measured elastic energy differed only slightly from the analytic result, $U_{\text{bend}}^{\text{cylinder}} = B\pi \approx 3.07 \times 10^{-4}$ Joule, where $B = Et^3/12(1-\nu^2)$ is the bending modulus, obtained using the thickness t, Young modulus E and Poisson ratio ν quoted above. The simulation gave an energy $\approx$ .01% larger than this. A discrepancy of this sign is expected because the analytic form neglects the small strain energy owing to the nonzero thickness of the sheet simulated.

References

[1] K. Krieger, “Extreme mechanics: buckling down”, Nature **488**, 146–147 (2012).

[2] K. Bertoldi, V. Vitelli, J. Christensen, and M. van Hecke, “Flexible mechanical metamaterials”, Nature Reviews Materials **2**, `10.1038/natrevmats.2017.66` (2017).

[3] C. D. Santangelo, “Extreme mechanics: self-folding origami”, Annual Review of Condensed Matter Physics **8**, 165–183 (2017).

[4] S. J. Callens and A. A. Zadpoor, “From flat sheets to curved geometries: origami and kirigami approaches”, Materials Today **21**, 241–264 (2018).

[5] E. Cerda and L. Mahadevan, “Conical Surfaces and Crescent Singularities in Crumpled Sheets”, Physical Review Letters **80**, 2358–2361 (1998).

[6] B. Davidovitch, Y. Sun, and G. M. Grason, “Geometrically incompatible confinement of solids”, Proceedings of the National Academy of Sciences **116**, 1483–1488 (2019).

[7] J. D. Paulsen, “Wrapping liquids, solids, and gases in thin sheets”, Annual Review of Condensed Matter Physics **10**, 431–450 (2019).

[8] E. Efrati, L. Pocivavsek, R. Meza, K. Y. C. Lee, and T. A. Witten, “Confined disclinations: exterior versus material constraints in developable thin elastic sheets”, Physical Review E **91**, 022404 (2015).

[9] E. Cerda and L. Mahadevan, “Geometry and Physics of Wrinkling”, Physical Review Letters **90**, 074302 (2003).

[10] E. Cerda, L. Mahadevan, and J. M. Pasini, “The elements of draping”, Proceedings of the National Academy of Sciences **101**, 1806–1810 (2004).

[11] T. Mora and A. Boudaoud, “Buckling of swelling gels”, Eur. Phys. J. E **20**, 119–124 (2006).

[12] M. M. Müller, M. B. Amar, and J. Guven, “Conical Defects in Growing Sheets”, Phys. Rev. Lett. **101**, 156104 (2008).

[13] Y. Klein, E. Efrati, and E. Sharon, “Shaping of elastic sheets by prescription of non-euclidean metrics”, Science **315**, 1116–1120 (2007).

[14] H. Vandeparre, M. Piñeirua, F. Brau, B. Roman, J. Bico, C. Gay, W. Bao, C. N. Lau, P. M. Reis, and P. Damman, “Wrinkling Hierarchy in Constrained Thin Sheets from Suspended Graphene to Curtains”, Physical Review Letters **106**, 224301 (2011).

[15] J. Hure, B. Roman, and J. Bico, “Stamping and wrinkling of elastic plates”, Physical Review Letters **109**, 054302 (2012).

[16] D. Vella, J. Huang, N. Menon, T. P. Russell, and B. Davidovitch, "Indentation of Ultrathin Elastic Films and the Emergence of Asymptotic Isometry", Physical Review Letters **114**, 014301 (2015).

[17] K. Miura, "Method of packaging and deployment of large membranes in space", The Institute of Space and Astronautical Science report, 1–9 (1985).

[18] L. Mahadevan and S. Rica, "Self-organized origami", Science **307**, 1740–1740 (2005).

[19] M. Schenk and S. D. Guest, "Geometry of miura-folded metamaterials", Proceedings of the National Academy of Sciences **110**, 3276–3281 (2013).

[20] B. Davidovitch, R. D. Schroll, D. Vella, M. Adda-Bedia, and E. A. Cerda, "Prototypical model for tensional wrinkling in thin sheets", Proceedings of the National Academy of Sciences **108**, 18227–18232 (2011).

[21] F. Brau, P. Damman, H. Diamant, and T. A. Witten, "Wrinkle to fold transition: influence of the substrate response", en, Soft Matter **9**, 8177 (2013).

[22] R. Levien, *The elastica: a mathematical history*, tech. rep. UCB/EECS-2008-103 (EECS Department, University of California, Berkeley, Aug. 2008).

[23] E. Cerda and L. Mahadevan, "Confined developable elastic surfaces: cylinders, cones and the elastica", Proceedings of the Royal Society A: Mathematical, Physical and Engineering Sciences **461**, 671–700 (2005).

[24] A. S. Pal, L. Pocivavsek, and T. A. Witten, *Faceted wrinkling by contracting a curved boundary*, 2022.

[25] M. P. do Carmo, *Differential Geometry of Curves & Surfaces* (Prentice Hall, 1976).

[26] S. C. Venkataramani, T. A. Witten, E. M. Kramer, and R. P. Geroch, "Limitations on the smooth confinement of an unstretchable manifold", Journal of Mathematical Physics **41**, 5107–5128 (2000).

[27] E. Efrati, E. Sharon, and R. Kupferman, "Buckling transition and boundary layer in non-euclidean plates", Physical Review E **80**, 016602 (2009).

[28] B. Audoly and Y. Pomeau, *Elasticity and geometry* (OUP Oxford, Jan. 2010).

[29] A. Lobkovsky, S. Gentges, H. Li, D. Morse, and T. A. Witten, "Scaling Properties of Stretching Ridges in a Crumpled Elastic Sheet", Science **270**, 1482–1485 (1995).

[30] S. Nechaev and R. Voituriez, "On the plant leaf's boundary, jupe à godets' and conformal embeddings", Journal of Physics A: Mathematical and General **34**, 11069–11082 (2001).

[31] T. A. Witten, “Stress focusing in elastic sheets”, Reviews of Modern Physics **79**, 643–675 (2007).

[32] K. A. Seffen and S. V. Stott, “Surface texturing through cylinder buckling”, Journal of Applied Mechanics **81**, `10.1115/1.4026331` (2014).

[33] H. Pham Dinh, V. Démery, B. Davidovitch, F. Brau, and P. Damman, “From Cylindrical to Stretching Ridges and Wrinkles in Twisted Ribbons”, Physical Review Letters **117**, 104301 (2016).

[34] G. Papazafeiropoulos, M. Muñiz-Calvente, and E. Martínez-Pañeda, “Abaqus2Matlab: A suitable tool for finite element post-processing”, Advances in Engineering Software **105**, 9–16 (2017).

[35] L. D. Landau and E. M. Lifshitz, *Theory of elasticity: volume 7*, edited by A. M. Kosevich and L. P. Pitaevskii, 3rd, Vol. 7 (Elsevier, Amsterdam, 1986).

[36] M. Smith, *Abaqus/cae 2018 user's manual* (Dassault Systèmes Simulia Corp, United States, 2018).

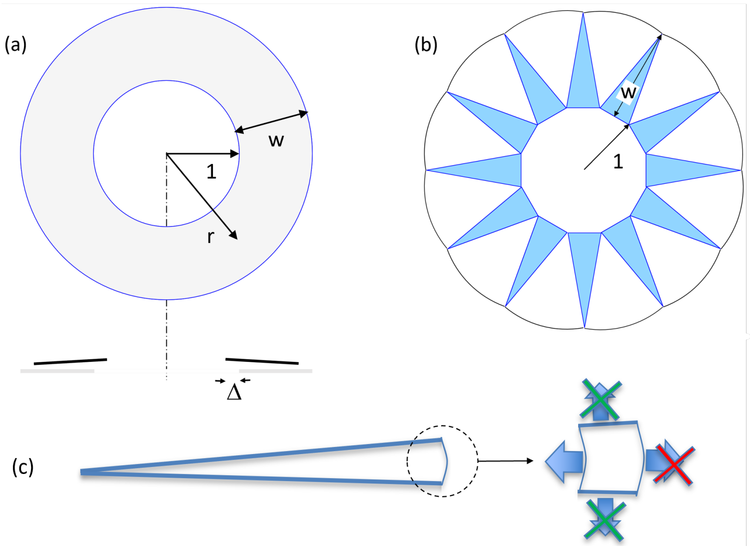

Figure 2.2: a) Sketch of the inner Lamé deformation of a horizontal annulus. (Top) Top view showing the undeformed annulus, of inner radius 1 and width w. (Bottom) Vertical cross-section of the deformed annulus through a line where the vertical displacement of the wrinkle is maximal. The undeformed state is shown in light shading; the dark lines are a section of the deformed annulus, contracted horizontally by a distance Δ. These lines are also displaced upward and tilted downward. b) Sketch of the circular-cone-triangle construction in its initial, flat state. Here, we choose wavenumber $m = 6$, hence it has 12 triangles (shown in colour). The mid-line and height w of one triangle are indicated. The sectors bridging the triangles are shown in white. When the bases of the triangles are moved inward, they must tilt to retain their shape and connectivity. The bridging sectors are squeezed laterally to form cones. A typical deformed example is shown in Fig. 2.1c. c) Top view of a narrow sector of the sheet, with detail of an area element at the outer edge of Lamé sheet showing radial (horizontal) and azimuthal (almost vertical) boundary forces. In the fully buckled (FT) regime [20], the azimuthal forces nearly vanish (as indicated by the upper and lower X's). In the the present "inner Lamé" system, the outer radial force also vanishes, indicated by the X at right. Thus, the inward radial force must also nearly vanish for force equilibrium. All elements to the left of the pictured one are subject to the same argument. Thus except for bending stresses, all radial stresses vanish.

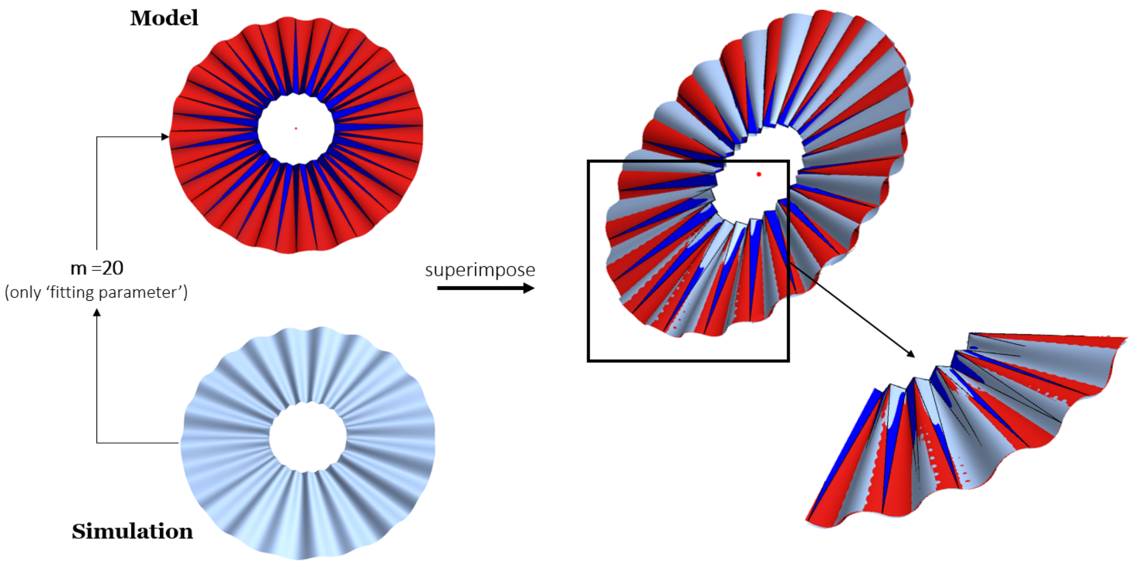

Figure 2.3: Qualitative comparison between simulation and our cone-triangle model for a representative sample ($w = 1.67$, $t = 1.33 \times 10^{-3}$). (Left) Given w, Δ and the wavenumber m from the numerical solution, we construct a model cone-triangle solution (cones in red, triangles in blue) using the procedure described in Section 2.3. (Right) For a qualitative comparison, we superpose the two solutions, with azimuthal rotation as the only degree of freedom. We find close agreement between them; with this top-down view, areas with colour indicate where the model solution is above the numerical solution, while those in grey indicate the opposite. In particular, the zoomed-in boxed portion shows close matching at both inner and outer boundaries. Zooming out to the whole annulus, we see that there is a 'phase mismatch' between the two solutions, with part of the solution in-phase (the boxed region) and part of it out-of-phase. This is due to the non-uniform size of the wrinkles in the numerical solution.

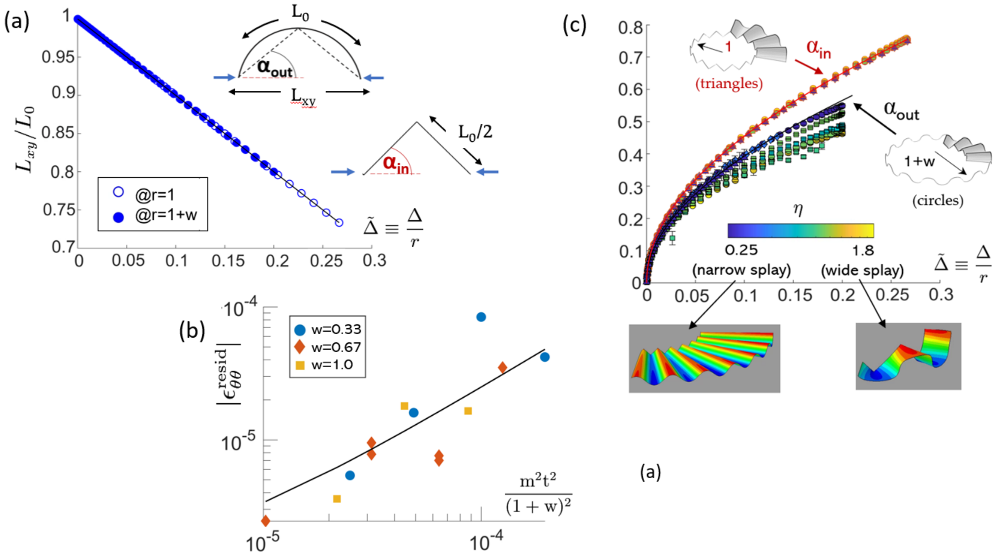

Figure 2.4: Comparisons of geometric quantities between theory and simulations (using the explicitly periodic initial conditions described at the beginning of Sec. 2.4). (a) Testing radial inextensibility. The main graph shows the evolution of the fractional projected length L_{xy}/L_0 of the material circles with increasing Δ, measured at both inner ($r = 1$) and outer ($r = 1 + w$) boundaries, for a representative sample ($w = 0.33$, $m = 25$, $t = 2.67 \times 10^{-4}$). The x-axis is the reduced variable $\tilde{\Delta} \equiv \Delta/r$. The measured values line up with the black line: $L_{xy}/L_0 = 1 - \tilde{\Delta}$. (inset) Sketches of the wrinkle profile at the two boundaries, showing the definition of lengths L_0 and L_{xy}, and slope angles α_{out} and α_{in}. The blue arrows indicate the compression direction. (b) Testing azimuthal inextensibility at the outer boundary. The magnitude of the residual azimuthal strain $|\epsilon_{\theta\theta}^{\text{resid}}|$ recorded slightly inside $r = 1 + w$, plotted logarithmically against the collective variable $m^2t^2/(1 + w)^2$ at large Δ, for multiple values of m, t and w. The black line shows the linear fit: $|\epsilon_{\theta\theta}^{\text{resid}}| \approx 0.24\frac{m^2t^2}{(1+w)^2}$. (c) Wrinkle slope angle vs. applied contraction $\tilde{\Delta}$ (see Sec. 2.42.4.2). (Top row) We separately test Eq. (2.3) for α_{in} (in red) and Eq. (2.4) for α_{out} (in black). The simulation data points are plotted alongside the model predictions. Simulated samples of differing width w and wavenumber m are coloured using the dimensionless cone splay parameter, $\eta \equiv \frac{\pi(1+w)}{mw}$. The error bars are standard deviations from averaging over all the wrinkles. Markers: $w = 0.33$ (circles), $w = 0.67$ (squares), $w = 1.0$ (diamonds), $w = 1.67$ (triangles). (Bottom row) Example wrinkle profiles for small and large η: (left) for $\eta = 0.25$ ($w = 1.0$, $m = 25$), and (right) for $\eta = 1.8$ ($w = 0.33$, $m = 7$). Colouring denotes height.

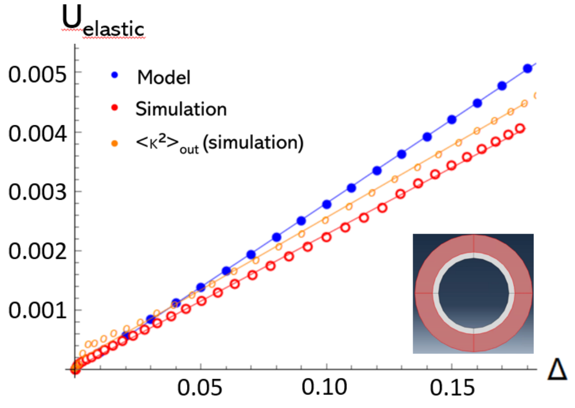

Figure 2.5: Comparing elastic energies (see Sec. 2.4.3) for a representative sample ($w = 1.0$, $m = 25$, $t = 6.67 \times 10^{-4}$): $U^{\text{sim}}_{\text{elastic}}(\Delta)$ (lower curve) ; see *Methods*) with $U^{\text{model}}_{\text{elastic}}(\Delta)$ (upper curve); Eq. 2.6) and $U^{\text{sim}}_{\langle\kappa^2\rangle}(\Delta)$ (middle curve); Eq. 2.5). All three curves show *Elastica*-like linear scaling (solid lines are fits), but the two theoretical curves overestimate the simulated energy by roughly 15% and 30% respectively. Other w and m values also generally overestimated the energies, as discussed in Sec. 2.42.4.3. Energy units are defined in *Methods*. (inset) Annulus, indicating the region where energies were compared (in red), omitting the high-curvature regions near $r = 1$.

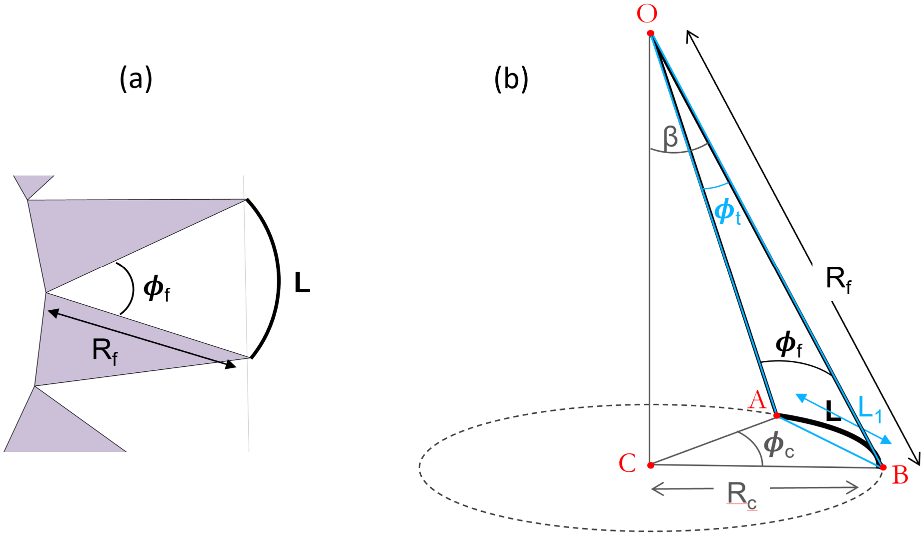

Figure 2.6: Isometrically constructing a sector of a cone from a flat arc sector. (a) The flat configuration. (b) The curved configuration; the actual conical sector and its variables are depicted in black, the triangle $\triangle AOB$ formed by the edges of the two adjacent tilted triangles, along with its variables, is in blue, and the putative cone with its variables is in grey.

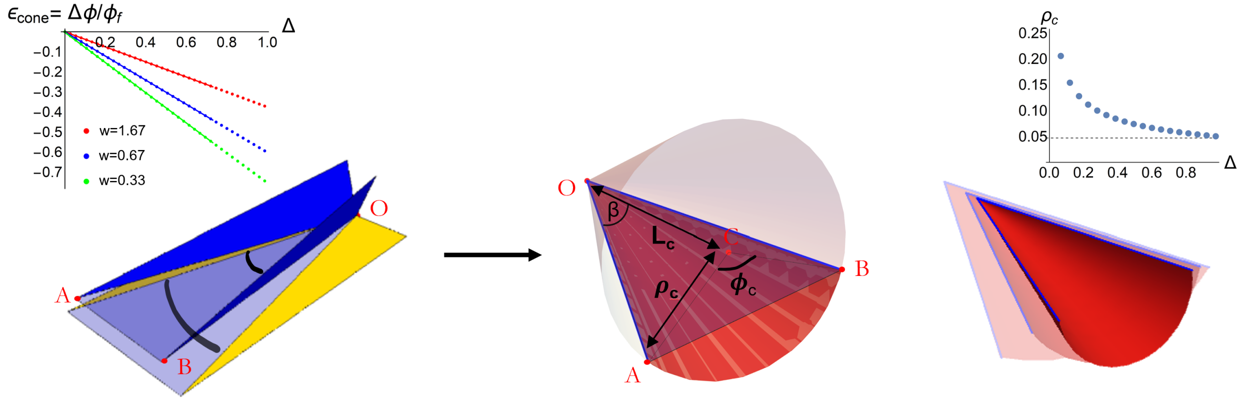

(a) (b) (c)

Figure 2.7: Constructing a single cone (see Sec. 2.3 and SI for details). (a) Two adjacent flat triangles (in yellow) subtending an angle ϕ_f, on tilting (in deep blue), subtend a smaller angle ϕ_t. Thus, the region between the triangles (shown approximately as a violet triangle) gets *squeezed* by an angle $\Delta\phi = \phi_t - \phi_f$. (inset) Evolution of the conical strain $\epsilon_{\text{cone}} = \Delta\phi/\phi_f$ with Δ for three different widths w. Model measurements are plotted alongside the predicted lines of slope $= -1/(1+w)$. (b) To fit within the contracted boundary defined by OA and OB, the region must bend into a circular cone of radius ρ_c, angular extent ϕ_c, axial length L_c and tilt angle β. The only ingredients needed for the construction are $\triangle AOB$ and the contraction Δ. (c) The evolution of the conical solution with Δ (here, $0.05 \leq \Delta \leq 0.6$). Greater opacity means larger Δ; the cones are translated with respect to each other for viewing clarity. (inset) As Δ increases, the radius of curvature ρ_c decreases, and for $\Delta \to 1$, attains an asymptotic value of $\rho_c \approx \frac{\pi w}{2m}$ (dotted line).

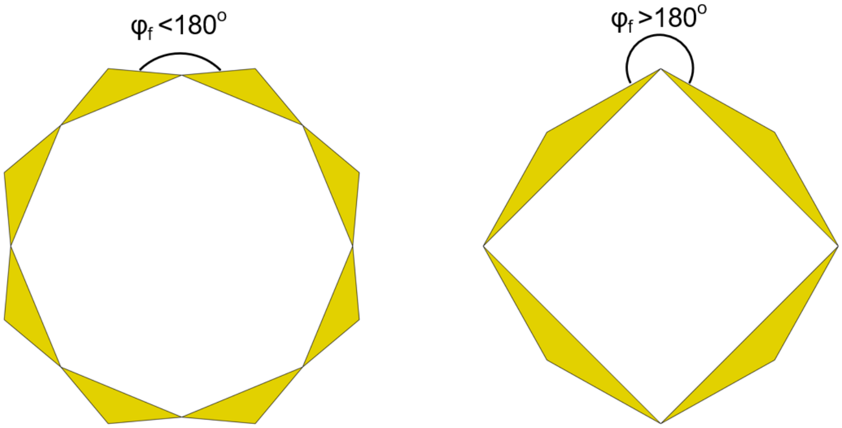

Figure 2.8: Two different flat state geometries for $w = 0.2$. (Left) For $m = 4$, the flat angle $\phi_f < \pi$, which allows the conical construction described in Sec. 2.7.3. (Right) For $m = 2$, the flat angle $\phi_f > \pi$, which means that our conical construction is not valid here.

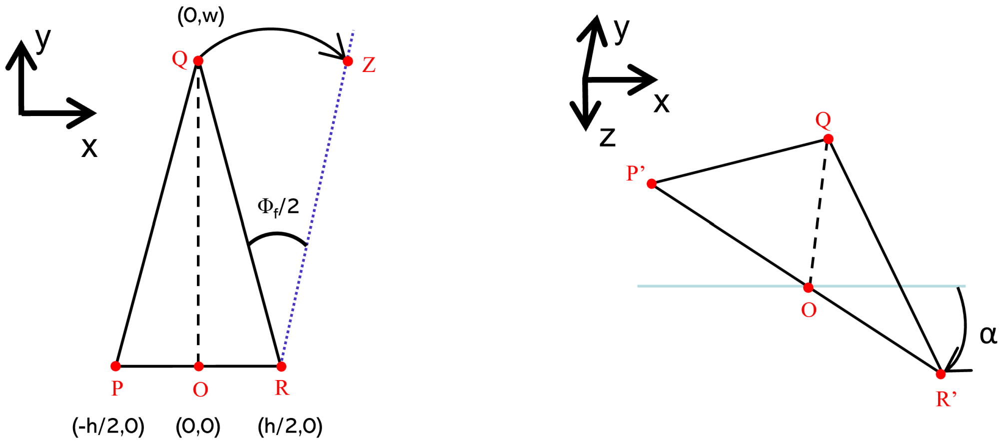

Figure 2.9: Diagram describing the geometric problem for determining ϕ_t. (Left) Top view of the flat isosceles triangle $\triangle PQR$ lying in the x-y plane, having height w and base h. OQ is the perpendicular bisector of PR. ϕ_f is the angle between QR and the dotted (vertical) blue plane. (Right) End view of the same triangle rotated clockwise by angle α about the y-axis.

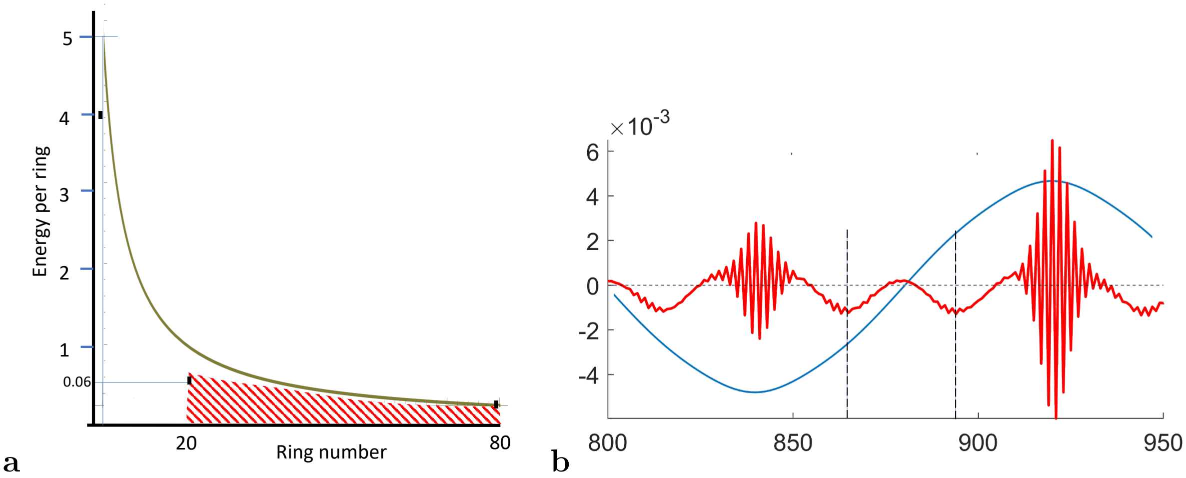

Figure 2.10: a) Energy distributions for the annulus of Fig. 2.5. Horizontal axis is radial distance from inner rim measured in finite element widths. Vertical axis is ring energy described in the text. Hashed region shows the region treated in Fig. 2.5. Its area represents the simulated energy with largest Δ on the lower curve of Fig. 2.5. Black marks show simulated ring energies at three selected radii. Solid curve shows the ring energy profile calculated from cone-triangle model used for the middle curve in Fig. 2.5. b) Simulated azimuthal strain $\epsilon_{\theta\theta}$ (in red) as a function of azimuthal finite-element coordinate θ, for a material circle located at the middle of an annulus with ($w = 0.33$, $t = 1.33 \times 10^{-3}$, $m = 10$, $\Delta = 0.27$). Light curve in blue shows height profile. Region spanning one trough and peak are shown. Variability of other troughs and peaks is similar. Vertical black lines indicate the location of two consecutive cone-triangle boundaries.

Chapter 3

The inner Lamé system: hysteretic wavelength selection

This chapter is a reproduction of the article "*Hysteretic wavelength selection in isometric, unsupported radial wrinkling*", authored by Anshuman S. Pal. The pre-print is available at `https://arxiv.org/abs/2211.12736`. The article is currently under peer review at the journal *Soft Matter*. This chapter reproduces the version initially submitted to the journal, with revisions responding to the initial referee reports. For the author's contribution to the paper, please refer to the *Preface* of this dissertation.

Abstract

In [Pal *et al.*, arXiv:2206.03552], the authors discuss how an unsupported flat annulus contracted at its inner boundary by fraction Δ, buckles into a radial wrinkling pattern that is asymptotically isometric and tension-free. What selects the wavelength in such a pure-bending configuration, in the absence of any competing sources of work? In this paper, with the support of numerical simulations, we argue that competition between stretching and bending energies at local, mesoscopic scales leads to the selection of a wavelength scale λ^* sensitive to both the width w and thickness t of the sheet: $\lambda^* \sim w^{2/3} t^{1/3} \Delta^{-1/6}$. This scale λ^* corresponds to an arrest criterion for wrinkle coarsening starting from any wavelength $\lambda \lesssim \lambda^*$, which can be interpreted in terms of both size and energetic barriers to further coarsening. However, the sheet can support coarser wavelengths: $\lambda \gtrsim \lambda^*$, since there is no penalty to their existence. Since this wavelength selection mechanism depends on the initial

value of λ, it is path-dependent or hysteretic.

3.1 Introduction

Thin elastic sheets under confinement buckle and bend to form a multitude of shapes. Perhaps the most ubiquitous of these forms of elastic pattern formation is *wrinkling*, viz. where the excess material length gets collected in multiple undulations. A central concern in the study of these structures is the determination of the wavelength λ of these undulations – which constitutes an *emergent* intermediate length scale, much smaller than the system size but much larger than the sheet thickness. Usually, this wavelength is selected [1] through competition between the sheet's bending stiffness and some external source of stiffness or deformation work, like a substrate [2], a tension field [3, 4], inertia [5], or even extrinsic curvature [6]. While the bending stiffness *promotes* larger λ in order to minimise wrinkle curvature, the substrate or other source of work tends to *penalise* large λ since it leads to large amplitude deformation. But how is wavelength determined in an unsupported sheet, i.e. in the absence of such external sources of stiffness?

A priori, an unconstrained sheet under compression should spontaneously choose the maximum wavelength possible – at the scale of the system size – in order to minimise bending energy. Thus, the minimum ingredient for generating an intermediate wavelength is the presence of some external *constraint*. Besides a substrate, another possible source of constraints is clamping at the boundary. References [7–9] study such systems where relatively coarse wrinkling in the bulk of the sheet gradually becomes refined in the proximity of a clamped or pinned boundary, in order to minimise the wrinkling amplitude. Of particular interest to us is Vandeparre et al. [9], which considers wrinkling in an *unsupported* rectangular sheet contracted at one boundary. Here, the wrinkle wavelength in the bulk is determined by the wavelength fixed (i.e. clamped) at the boundary, coarsening outward through a 'wrinkle hierarchy' (see Figs. 3.2b and 3.4a). But what if the sheet is *unsupported and also unclamped*?

In this paper, we address the question of wavelength determination in precisely such a case, using the geometry reported in reference [10] [1]. The system considered there is a variant of the classic Lamé radial wrinkling deformation (see Figs. 3.1a and b), where we contract the inner boundary of a circular annulus through a radial displacement Δ, keeping the outer boundary free. We call this the "inner Lamé" system. Importantly, this inner boundary is kept *unclamped* and *unpinned*, i.e., it is free to both displace and rotate out-of-plane. In [10], we show that such boundary-induced contraction of the annulus generates a pattern of

---

[1] This reference is reproduced as Chapter 2 in this dissertation

uniform radial wrinkling that becomes *isometric* (i.e., unstretched) as the thickness becomes much smaller than the wavelength. Thus, in this limit, its radial tension field is negligible as compared to that of a similarly deformed classical Lamé annulus [4]. However, even in this isometric and "tension-free" limit, where there should be no dependence on thickness, the wrinkling deformation selects a wavelength that is observed to depend on both the sheet thickness t and width w (see Fig. 3.1d).

In this paper, we show that this wavelength is consistent with a similar coarsening mechanism as in Vandeparre et al. [9], but without any spatial hierarchy involved. Rather, the coarsening takes place progressively over the course of the deformation (see Fig. 3.1c), and is arrested due to the non-zero stretching energy associated with 'wrinklons' – Y-shaped spatial features where two wrinkles merge into one – which constitute the basic unit of the coarsening process. Thus, *arrested coarsening* determines the final wavenumber (i.e., the number of wrinkles) m^* in the sheet. However, if the sheet manages to attain a coarser wavenumber $m < m^*$ by any means (e.g., manual setting by the experimenter), then it stays there. Thus, the wavelength selection depends on initial conditions, and can be considered *hysteretic* or path-dependent. These are the central results of this paper.

Below, we derive the discussed arrest criterion for the wavelength selection and demonstrate its viability numerically. The paper is organised as follows. Section 3.2 defines the inner Lamé deformation that we simulate, and the numerical methods we use to this end. In Section 3.3, we state the main results of this paper, deriving a scaling law for the critical arrest wavelength, $\lambda^* \sim 1/m^*$ (the black line in Fig. 3.1d), and argue that it causes hysteretic wavelength selection. Finally, Section 3.4 discusses the significance of these results.

3.2 Methods

The system under consideration here is sketched in Fig. 3.1a. We start with a flat circular annulus of width w and thickness t, whose initial inner radius we take as our unit of length. To deform this annulus, we pull the inner boundary radially inward by a distance Δ, so that it is forced to live on a cylinder whose radius is reduced by Δ. This leads to a *contraction* of the inner boundary by a factor of Δ, and the equilibrium shape of the sheet thus obtained is the radial wrinkling shown in Fig. 3.1b. The system can thus be conveniently defined using only three geometric parameters: thickness t, width w, and (dimensionless) radial contraction Δ. The internal forces determining the shape arise from the in-plane stretching modulus $Y = Et$, and the bending modulus $B = Et^3(1-\nu^2)/12$, where E and ν are the material's Young's modulus and Poisson ratio, resp. In thin sheets with thickness t much smaller than the inner radius and the width w, the sheet may be taken as virtually unstretchable, and many features of the shape are independent of Y [4]. Indeed, in [10], we show that the radial wrinkling morphology under study here (see Fig. 3.1b) is *geometrically*, i.e. developably, isometric (as opposed to the class of asymptotic, non-developable isometries discussed in [1] and references therein). The macroscopic energy thus lives purely in the bending mode.

3.2.1 Numerical methods

To investigate the wrinkling morphology of the inner Lamé system here, we use the same numerical methods used in [10]. For our simulations, we used the commercial finite-element (FE) solver Abaqus 2018 (SIMULIA, Dassault Systèmes). We used a protocol in which we gradually displaced the boundary in time, allowing the system to relax quasi-statically, such that the rate of motion of the boundary does not affect the emergent shape or its energy. The forward time integration was done using one of two standard FE protocols – 'dynamic, explicit' and 'dynamic, implicit' – both being found to give comparable results. Such dynamic integration protocols introduce inertia into the simulation, which is essential for accurately tracking local minima through instabilities and bifurcations, and thus finding reliable post-buckling solutions [11]. In contrast, static (i.e., zero inertia) simulation protocols are known to remain stuck in local minima near the initial conditions, and far away from the true minimum [11]. However, to avoid gross kinetic effects in the presence of inertia, we made sure to increase the contraction Δ slowly enough such that the kinetic energy of the system always remained $\lessapprox 5\%$ of the elastic energy. This is standard procedure for quasi-static analyses in finite-element simulations. The FE simulation details are given in depth in the SI of [10]. Here, we give a brief overview.

To simulate the inner Lamé system, we used its defining boundary conditions: radial displacement $e_r(r = 1) = -\Delta$ at the inner boundary, and the outer boundary at $r = 1 + w$ free. We chose to apply a maximum contraction of $\Delta_{\max} = 0.267$ at the inner boundary. All observed coarsening and selection in our simulations occurs for Δ much smaller than this maximum (see Fig. 3.1c); increasing Δ further within this range only changes the amplitude without affecting the wavenumber. We did not extend the range enough to observe the anticipated weak dependence on Δ.

To account for the possibility of high strains at such large contractions, the sheet was modelled as a Neo-Hookean hyperelastic material with coefficients equivalent to the linear moduli: Young's modulus, $E = 0.907125$ MPa, and Poisson ratio, $\nu = 0.475$, corresponding to a rubber-like material. To verify that results are independent of the material model, we also re-performed several simulations with a linear material model with these same moduli.

To test the validity of our results over a range of parameters, we kept the inner radius fixed and varied the other two parameters – width w and thickness t – over the range of a decade. For the width, we used values $w = 0.20, 0.33, 0.67, 1.0, 1.67$ (a factor of almost 10, ranging from very narrow to moderately wide), and for thickness, we used values $t = 2.67 \times 10^{-3}, 1.33 \times 10^{-3}, 6.67 \times 10^{-4}, 2.67 \times 10^{-4}, 1.33 \times 10^{-4}$ (a factor of 20, ranging from moderately thick to very thin). We performed consistency checks to ensure that the final morphology was independent of the choice of any simulation parameters.

3.2.2 Boundary conditions

As noted in the Introduction, the specifics of the wrinkling morphology depend strongly on how the contracted boundary is constrained. Clamping the boundary leads to the wrinkling hierarchy morphologies discussed in [9] (see also Figs. 3.2b and 3.4). The other extreme is to allow each point on the boundary circle to lie anywhere on the confining cylinder; such boundaries lead to wrinkling only in a transient regime, leading ultimately to collapse into a macroscopic fold. Here we study an intermediate constraint in which points on the bounding circle may displace only axially (i.e. vertically) on the bounding cylinder; azimuthal (θ) motion is not allowed. Doing so automatically prohibits folding (since this requires lateral motion), but without interfering with the wrinkling.

3.2.3 Obtaining sinusoidally-biased flat states

In Sec. 3.3.2, we use starting configurations with a pre-determined wavelength at the outer boundary, λ_{init}. To obtain these, we biased the initial flat state with linear perturbations (of amplitude $\sim 10^{-4} - 10^{-3}$) of sinusoidal modes of known wavenumber m. These modes were obtained using standard linear eigenmode analysis methods in Abaqus [12].

3.3 Results

The elastic energy of the wrinkled annulus, as found in [10], is dominated by bending. Thus, it favours the coarsest possible wrinkling. However, from Fig. 3.1d, we see that the observed wavenumber m^* in the system becomes indefinitely large as we decrease thickness t or width w. Thus, there exists some 'constraint' (generically speaking) that competes with the bending energy to select the intermediate wavenumbers m^*. In this section, we consider this selection mechanism.

In what follows, instead of simply counting the number of wrinkles m in the annulus, we measure the *continuous* (in-plane) wavelength λ at the outer boundary, averaged over multiple wrinkles of the sample. [2] The standard deviation in λ then also gives a measure of the non-uniformity of wrinkling, something which the integer m cannot capture. Thus, in what follows, we aim to predict the continuous variable λ^*, related to the counted m^* by the approximate relationship: $\lambda^* \approx 2\pi(1+w)/m^*$.

3.3.1 Wrinklons and arrested coarsening

We first note that the selection of the final wavenumber in a simulation is not an instantaneous process. Figs. 3.1c and 3.2b show that, as we apply the contraction $\Delta > 0$, the flat annulus initially buckles to form fine-scale radial wrinkling. This then coarsens rapidly, reducing the bending energy, but with the coarsening stopping at some final wavenumber $m^* \sim 1/\lambda^*$. This suggests that there is a continuous 'path' from the initial fine value of λ to the final value λ^*, but not beyond. Here, we argue that this path is blocked because a further coarsening becomes energetically unfavourable. In other words, the coarsening process gets energetically *arrested*.

The coarsening process is controlled by the Y-shaped spatial features named 'wrinklons' [9], which form every time two wrinkles merge into one. In what follows, we discuss the energetics of wrinklons, approximating the wrinkles as being rectilinear (as in Fig. 3.2a), and ignoring any radial splay. We discuss the accuracy of this assumption in Sec. 3.4. The energetics of a wrinklon is closely associated to its shape. Fig. 3.2a shows the geometry of a wrinklon using an origami model (adapted from [9]). Here, the paper sheet is creased to have wavelength λ on the right and 2λ on the left. The transition zone is the wrinklon. As can be seen from the cut in the sheet, this involves non-zero extension of the material: to allow a trough in the λ wave on the right to rise up to the peak of the 2λ wave on the left, a horizontal length L (see inset of Fig. 3.2d) must be stretched into the hypotenuse $\sqrt{(2\zeta)^2 + L^2}$, where ζ is the amplitude of the λ-wave. For small slope ζ/L, this generates a strain of order $(\zeta/L)^2$. In the absence of a substrate or boundary tension, this contributes a stretching energy density $\sim Y(\zeta/L)^4$, where Y is the stretching modulus.

In [10], we show that the wrinkling under consideration is isometric. In this strain-free limit, we can use the constraint of inextensibility (i.e., length conservation) to relate the average slope ζ/λ of the wrinkled circles to the applied contraction Δ. Taking this latter to be constant over the length of the wrinklon, for small slopes, we have: $(\zeta/\lambda)^2 \sim \Delta$. This is popularly known in literature as the 'slaving condition' [1], since it shows that the amplitude ζ and wavelength λ are co-dependent variables for inextensible wrinkling. Thus, removing ζ

---

[2] It also allows us to take measurements for only half or quarter of the annulus. This makes data extraction faster.

in favour of λ and Δ, the elastic energy of a wrinklon of area $\sim L\lambda$ is given by:

$$U_{\text{wrinklon}} \sim Y\lambda^5 L^{-3}\Delta^2. \tag{3.1}$$

To see how such wrinklons can select the wavelength, consider the following picture of kinetic arrest. Assume uniform wrinkling of wavelength λ over the entire width w of the sheet. Then this wavelength can coarsen further if and only if a wrinklon can form. This will happen if and only if there is a decrease in the net elastic energy during this process. Since there is an energy gain from creating the wrinklon, as well as a bending energy decrease due to wrinkle coarsening from $\lambda \to 2\lambda$, the net change in energy δU is:

$$\delta U(\lambda) = U_{\text{wrinklon}}(\lambda) - \delta U_{\text{bend}}(\lambda), \tag{3.2}$$

where $\delta U_{\text{bend}}(\lambda) \sim B\Delta w\lambda^{-1}$ for an area $\sim \lambda w$. Thus, a wrinklon will form, and the wavelength will increase, only if $\delta U(\lambda) < 0$. Setting $\delta U(\lambda) = 0$ then gives us a critical minimum scale $L^*(\lambda)$ (using Eq. 3.1):

$$L^*(\lambda) \sim t^{-2/3}\Delta^{1/3}w^{-1/3}\lambda^2, \tag{3.3}$$

such that only wrinklons having length $L > L^*(\lambda)$ are energetically feasible in the system, i.e., they lower the net energy: $\delta U(\lambda) < 0$. Since the wrinklon has to be smaller than the sheet's width as well, we find that wrinklons can form as long as their size L obeys the bounds: $w > L > L^*(\lambda)$.

However, each round of coarsening, as λ increases, Eq. 3.3 shows us that $L^*(\lambda)$ also increases (rapidly). Thus, when $L^*(\lambda) > w$, there can be no wrinklon that reduces the energy, so that no further coarsening can occur. This defines a critical wavelength scale λ^* such that

$$L^*(\lambda)|_{\lambda^*} = w. \tag{3.4}$$

Using Eq. 3.3, we get:

$$\lambda^* \sim w^{2/3}t^{1/3}\Delta^{-1/6}. \tag{3.5}$$

The conclusion is that all wavelengths λ with $L^*(\lambda) < w$, and thus $\lambda \lesssim \lambda^*$, are susceptible to wrinklon-mediated coarsening, and are hence unstable and *should not be visible* in the sheet. Moreover, these finer wavelengths should get coarsened up to or right above the critical wavelength λ^*; beyond this, coarsening is energetically unfeasible and gets arrested. This is confirmed in Fig. 3.1d, where the best-fit λ^* line is drawn in black (henceforth, we call this the 'wrinklon line').

Eq, 3.5 is the central prediction of this paper. It emerges directly from Eq. 3.4, which represents an arrest criterion for wrinklon-mediated coarsening in the annulus. This shows that *transient* wrinklons in the inner Lamé system can select a wavelength by a mechanism of kinetic arrest. This wavelength is an emergent phenomenon depending on all three geometric factors t, w and Δ, but independent of material constants E and ν. Eq. 3.5 predicts wider and thicker sheets to display coarser wrinkling, and vice versa for narrower, thinner sheets. On the other hand, the arrest argument above also suggests that wavelengths coarser than λ^* should remain stable since they are not subject to further coarsening via wrinklons. Our next step is thus to confirm the possibility of the sheet supporting wavelengths $\lambda \gtrsim \lambda^*$.

3.3.2 Attaining coarser wavelengths by changing initial wavelength

The natural tendency of the wrinkled annulus is to minimise its bending energy and coarsen as much as possible. The arrest argument above suggests that, *using wrinklons*, the wrinkling cannot coarsen beyond λ^*. However, given an opportunity to bypass the wrinklon mechanism and coarsen directly, the annulus should do so.

One way to test this hypothesis is to *manually* set a coarser wavelength in our simulations. We do this by biasing the initial flat state with a sinusoidal perturbation of known wavenumber (see Sec. 3.2.3). In Fig. 3.3a, we show the results of this method. The blue and magenta dots are the same data points from Fig. 3.1c, obtained by contracting the annulus from a flat state (which has $\lambda_{\text{init}} \ll \lambda^*$) or a state biased with sinusoidal modes having $\lambda_{\text{init}} \lesssim \lambda^*$. They all lie on the black "wrinklon line": $\lambda = \lambda^*$. On the other hand, the new green dots are obtained by starting from a biased state whose wavelength at the outer boundary obeys $\lambda_{\text{init}} \gtrsim \lambda^*$. We find that, on average, these samples do not coarsen at all. In other words, they are not susceptible to the wrinklon coarsening mechanism. Indeed, we used this method in [10] to generate uniformly wrinkled patterns to provide clean geometric data. Thus, Fig. 3.3a is fully consistent with the hysteretic picture posited at the end of Sec. 3.3.1

An independent way of affirming this λ-dependent coarsening is by traversing the wrinklon line horizontally. We do this by fixing the initial wavelength λ_{init} and width w, and varying the thickness t. In Fig. 3.3b, we plot some representative data points, showing both λ_{init} (empty symbols) and the final wavelength λ_{final} (full symbols) for these samples. We see that the leftmost (i.e. thinnest) samples, which start above the wrinklon line, do not coarsen. However, as soon as we cross the wrinklon line horizontally (following the dotted grey line), the samples start to coarsen, i.e., they move straight up. As expected, the coarsening happens up to or above the wrinklon line, consistent with the discussion in Sec. 3.3.1.

3.3.3 λ^* starting from wrinkle hierarchy

While the previous two sub-sections suffice to describe the central results of this paper, it is instructive to see the selection of λ^* from a different perspective, as emerging smoothly from the modification of a more constrained version of the inner Lamé system. In this version, we pin the inner boundary ($r = 1$), prohibiting any vertical, out-of-plane displacement. Applying contraction Δ with such *pinned* boundary conditions (BCs) then leads to the creation of a spatial wrinkle-hierarchy morphology (see Fig. 3.4b) – like the ones studied in [7–9] for rectangular geometries – where fine-scale wrinkling at the pinned boundary coarsens progressively in space via multiple generations of wrinklons. Despite the qualitatively different morphologies between the pinned and unpinned cases (see Fig. 3.4), we argue that one should still expect the wavelengths at the outer boundary for the two cases to be the same. To see this, consider the following.

We can think of the emergence of the unpinned morphology in Fig. 3.4a starting from the pinned, wrinkle-hierarchy case in Fig. 3.4b. Eq. 3.1 tells us that wrinklons cost non-zero elastic energy. Moreover, they separate a region of fine, higher-energy wrinkling (nearer $r = 1$), from a region of coarser, lower-energy wrinkling (nearer $r = 1 + w$). Thus, allowing the wrinklons to move right up to the inner boundary would eliminate not only the wrinklons themselves but also the entire fine wrinkling region, leading to a net lowering of the sheet's energy.

Imagine gradually undoing the pinning at $r = 1$ in Fig. 3.4b, allowing the boundary nodes to displace vertically within a maximum height ϵ. As ϵ increases, the boundary will be able to support coarser wavelengths. Thus, as it reaches the approximate height of the innermost generation of wrinklons, in order to minimise elastic energy, these wrinklons should all migrate to the boundary and disappear, thereby increasing the wavelength at $r = 1$ by a generation. Similarly, when ϵ reaches the height of the second (now innermost) wrinklon generation, this generation should also vanish in a similar manner, decreasing the energy and coarsening the wavelength by a further generation. As ϵ increases further, this coarsening process may continue as long as there are wrinklons that can move into the inner boundary. That is, as long as there are more inner wrinkles than outer ones. The end point of this process is thus a state where the original outer wrinkles extend to the inner boundary. Thus, we would reach the unpinned boundary conditions of the original inner Lamé system, and anticipate the same morphology (i.e. Fig. 3.4a). This argument tells us that we should expect:

$$\lambda^* = \lambda_{\text{hierarchy}}(x = w), \tag{3.6}$$

where $\lambda_{\text{hierarchy}}(x)$ is the wavelength at distance x from the pinned boundary in the wrinkle hierarchy. Using the expression

$$\lambda_{\text{hierarchy}}(x) \sim x^{2/3} t^{1/3} \Delta^{-1/6} \tag{3.7}$$

given for rectangular geometries in Vandeparre et al. [9], we recover Eq. 3.5 for λ^*. To verify the prediction of Eq. 3.6, we perform simulations of this pinned BC for our annular systems to measure $\lambda_{\text{hierarchy}}(x = w)$. We then compare $\lambda_{\text{hierarchy}}(x = w)$ to λ^* measured for the unpinned case. We find that our measurements are fully consistent with Eq. 3.6. We can already see this qualitatively in the bottom row of Fig. 3.4. Fig. 3.1d shows this quantitatively: λ^* and $\lambda_{\text{hierarchy}}(x = w)$ measured for a wide range of samples with varying w, t and Δ, collapse on to the same straight line given by Eqs. 3.5 and 3.7. The "unpinned-hierarchy" argument for λ^* described in this section thereby provides an independent confirmation of the arrest criterion argument presented in Secs. 3.3.1 and 3.3.2.

3.3.4 Summary

The results presented in Sec. 3.3 together paint the following story. First, the radially-contracted inner Lamé system, despite having its energy dominated by only bending, selects a critical wavelength scale λ^* much finer than the system size. This λ^* is determined through competition between stretching and bending energies at the scale of local features called wrinklons. Second, the selected λ^* is a function of the single collective variable $w^{2/3}t^{1/3}\Delta^{-1/6} \equiv \tilde{x}$, sensitive to both the smallest (thickness t) and largest (width w) dimensions of the sheet. Third, the wavelength selection is hysteretic (i.e. path-dependent), since the final wavelength λ selected by the annulus depends on its initial location in the $\lambda - \tilde{x}$ plane. As seen in Fig. 3.3a, the critical wavelength λ^* acts as a linear discriminant in this plane, separating it into two regions. Consistent with its desire to minimise bending energy, the sheet can support wavelengths coarser than λ^* but nothing finer than it. Thus, the wavelengths supported by the sheet obey the inequality: $\lambda \gtrsim \lambda^*$.

3.4 Discussion

3.4.1 Significance

The mechanism of *wrinklon-mediated arrested coarsening* presented in this paper accounts for all the qualitative and quantitative features of the wavelengths λ measured in our inner Lamé samples. The novelty of this mechanism must be stressed. The *hysteretic* wavelength selection paradigm presented here is very different from the traditional paradigms of wavelength selection in elastic wrinkling, which are based on global energy minimisation and hence are path-independent. For example, consider the prototypical case of wrinkling in a thin sheet of bending stiffness B attached to a substrate of stiffness K [3][3]. Competition between the bending of the sheet and the deformation of the substrate leads to the selection of a wavelength $\lambda_{\text{substrate}} \sim (B/K)^{1/4}$ that minimises the global energy. $\lambda_{\text{substrate}}$ here does not depend on the initial value of the wavelength chosen. If we start with a putative wavelength $\lambda' \lesssim \lambda_{\text{substrate}}$, then bending energy will force the wavelength to increase to $\lambda_{\text{substrate}}$. Conversely, if we start with some $\lambda' \gtrsim \lambda_{\text{substrate}}$, then the substrate energy will force the wavelength to decrease to $\lambda_{\text{substrate}}$. Thus, on a plot of λ vs. $(B/K)^{1/4}$, data points measured from samples with different values B and K should all lie on a single straight *line*.

In contrast, in the inner Lamé system, the lack of a macroscopic force to compete with the sheet's bending energy means that there is no global energy minimum. Instead, the wavelength is selected through *local* competition at wrinklon-scale between bending and *stretching*, this latter being the only source of competition possible in an unsupported sheet. The observed one-sided hysteresis is a direct consequence of this energy balance at scale L^*. Bending energy wants to coarsen wavelengths as much as possible, but the size of the sheet w acts as a fundamental barrier to this coarsening, through the "coarsening condition": $L^*(\lambda) \leq w$. Conversely, the lack of a (real or effective) substrate means that there are no penalties to wavelengths coarser than λ^*. Thus, on the $\lambda - \tilde{x}$ wavelength plane, there is an entire *range* of wavelengths available to the sheet: $\lambda \gtrsim \lambda^*$.

Thus, in a fundamental but non-trivial way, the wavelength λ in the inner Lamé system is selected by the sheet's size w. This is similar and yet dissimilar to known cases of geometric wavelength selection in isometrically buckled systems, where *both* macroscopic stretching and bending are absent. A good example is the faceted twisted ribbon in [13]), which buckles into a periodic pattern of triangular facets. Here, the wavelength is directly set by the ribbon's width w: $\lambda = w$ [13]. Our hysteretic wavelength selection also involves the sheet width, but through an *inequality*. In this sense, it is a weaker and less restrictive geometric selection principle.

3.4.2 Generalisation

An expected consequence of such a simple size-based selection principle is that it should *generalise* to other cases as well, provided wrinklons are the dominant wavelength-selection mechanism. For example, consider wavelength selection in a common hanging curtain. A curtain is not only rectangular, but also subject to a vertical tension field in the form

---

[3] In terms of the quantities already introduced in this paper, K has units of $Y/(\text{length})^2$ or $B/(\text{length})^4$.

of gravity. Due to this weight-induced tension, we would expect L^* in curtains to scale differently [9] from our tension-free case (Eq. 3.3). However, irrespective of the scaling, [9] shows that the outer wavelength in a hanging curtain is selected by wrinklons. Then our size-based wavelength selection principle has the following implication. Let the curtain be of height h, and its manually fixed wavelength at the top boundary be λ_0. If λ_0 is coarse enough that $L^*(\lambda_0) > h$, then there should be no wrinklons in the curtain, and we should see a uniform wrinkling pattern with wavelength λ_0. However, if we decrease λ_0 gradually, then we should find wrinklons forming as soon as $L^*(\lambda_0) \approx h$, with a consequent doubling of the wavelength at the outer boundary. Such a concrete prediction for a crossover can be easily verified through experiments.

We also note that the scaling law Eq. 3.5 for λ^* accounts for all the parameters in our inner Lamé system. Thus the ratio of λ^* to $\tilde{x}$ is a pure number (estimated to be ≈ 2.2) that should be the same even for more general cases of unsupported, inner boundary-contracted annuli (with free outer boundary). In Sec. 3.3, we have shown Eq. 3.5 to hold for the case of a pinned inner boundary, as well as an inner boundary that moves radially inwards. In Sec. 3.2.2, we mention the case where the boundary is free to move even azimuthally along the constraining cylinder, and shows folding. In this case, the persistence of the wrinkles extends to the time scale where boundary points on the material can migrate azimuthally over a finite fraction of the circumference. We would expect Eq. 3.5 to be valid in this transient regime. Finally, we might expect Eq. 3.5 to hold even for cases where the inner boundary is contracted in a different manner, e.g., when it is forced to live on a constraining cone instead of a cylinder. However, the numerical pre-factor need not be the same in this case.

3.4.3 Remarks

Certain features of our results in Sec. 3.3 deserve comment. First, we note that both derivations of the threshold λ^* (viz., Eqs. 3.5 and 3.6) ignore any splay in the wrinkle structure arising from the overall annular geometry of the system. The fact that our measurements coincide with the prediction thus suggests that wrinkle splay is unimportant in the regime of w, t and Δ considered here. We would expect such splay to become important particularly for large width w. Second, in Figs. 3.3a and b, we note that the data points which have coarsened up to the wrinklon line λ^* from below show considerable dispersion. The data points reflect the mean outer λ, averaged over all wrinkles in an annulus; in Fig. 3.3b, we add error bars to additionally depict the imprecision in λ for a sample. Such variability can be explained partially by two factors. The first is that the real simulation wavenumber m must be an integer, and thus any wrinklon that migrates to the inner boundary must change m by -1. This will correspond to jumps, and hence dispersion, in the measured outer wavelength $\lambda \sim 1/m$. The second factor to consider is the random nature of the coarsening events. All wrinklons do not coarsen simultaneously (thereby changing $m \to m/2$ directly). Instead, wrinklons form randomly and wrinkle-pair-by-pair, with wrinkle pairs separated in space, *a priori*, coarsening independently. This leads to m decreasing in smaller steps (see Fig. 3.1c), and also to heterogeneity in the wrinkles and wrinklons (see Fig. 3.4b and the error bars in Fig. 3.3b). The energetic inequality $\delta U < 0$ (see Eq. 3.2) only marks the feasibility regime for such coarsening events to occur. Consequently, if coarsening is an equal probability event for each wrinkle pair, then one should expect a larger drop in m, i.e. more coarsening, if the configuration starts out with a larger initial m. We see that, among the coarsened data points in Fig. 3.3b, the red dots ($w = 0.33$) show noticeably large coarsening. This discrepancy might then be related to the fact that these samples started from biased states with a relatively large initial wavenumber $m_{\text{init}} \approx 25 - 35$, compared to $m_{\text{init}} \approx 15 - 20$ for the wider samples (green and teal symbols). We note, moreover, that the sign of the discrepancy in Fig. 3.3b is generally such that the data points lie *above* λ^*. This is consistent with our claim that λ^* only acts as a *lower threshold* to the wavelengths observable in the system: $\lambda \gtrsim \lambda^*$.

Finally, we recall that [10] shows the inner Lamé wrinkle configuration to be isometric, i.e., to have only bending energy. On the other hand, in this paper, we use stretching energy to explain the wavelength selection. This might seem paradoxical, but is so only at first glance. The stretching energy of the wrinklon defines an energy barrier that would need to be crossed in order to increase the wavelength beyond $\lambda *$. It does not influence the energy of the state for a given λ (equivalently, a given m), which as shown in [10] is unrelated to this barrier.

Conflicts of interest

There are no conflicts to declare.

Acknowledgements

The author would like to thank Benny Davidovitch and Enrique Cerda for many insightful discussions, and Luka Pocivavsek, Nhung Nguyen and George Papazafeiropoulos for help with numerical analysis. This work was done in pursuit of a PhD under the supervision of Prof. Thomas A. Witten. This work was primarily supported by the University of Chicago

Materials Research Science and Engineering Center (MRSEC), funded by National Science Foundation (NSF) grants DMR-1420709 and DMR-2011854, the latter in the form of a UChicago-MRSEC student fellowship.

References

[1] J. D. Paulsen, "Wrapping liquids, solids, and gases in thin sheets", Annual Review of Condensed Matter Physics **10**, 431–450 (2019).

[2] N. Bowden, S. Brittain, A. G. Evans, J. W. Hutchinson, and G. M. Whitesides, "Spontaneous formation of ordered structures in thin films of metals supported on an elastomeric polymer", Nature **393**, 146–149 (1998).

[3] E. Cerda and L. Mahadevan, "Geometry and Physics of Wrinkling", Physical Review Letters **90**, 074302 (2003).

[4] B. Davidovitch, R. D. Schroll, D. Vella, M. Adda-Bedia, and E. A. Cerda, "Prototypical model for tensional wrinkling in thin sheets", Proceedings of the National Academy of Sciences **108**, 18227–18232 (2011).

[5] F. Box, D. O'Kiely, O. Kodio, M. Inizan, A. A. Castrejón-Pita, and D. Vella, "Dynamics of wrinkling in ultrathin elastic sheets", Proceedings of the National Academy of Sciences **116**, 20875–20880 (2019).

[6] J. D. Paulsen, E. Hohlfeld, H. King, J. Huang, Z. Qiu, T. P. Russell, N. Menon, D. Vella, and B. Davidovitch, "Curvature-induced stiffness and the spatial variation of wavelength in wrinkled sheets", Proceedings of the National Academy of Sciences **113**, 1144–1149 (2016).

[7] B. Davidovitch, "Period fissioning and other instabilities of stressed elastic membranes", Physical Review E **80**, 025202 (2009).

[8] R. D. Schroll, E. Katifori, and B. Davidovitch, "Elastic building blocks for confined sheets", Physical Review Letters **106**, 074301 (2011).

[9] H. Vandeparre, M. Piñeirua, F. Brau, B. Roman, J. Bico, C. Gay, W. Bao, C. N. Lau, P. M. Reis, and P. Damman, "Wrinkling Hierarchy in Constrained Thin Sheets from Suspended Graphene to Curtains", Physical Review Letters **106**, 224301 (2011).

[10] A. S. Pal, L. Pocivavsek, and T. A. Witten, *Faceted wrinkling by contracting a curved boundary*, 2022.

[11] M. Taylor, B. Davidovitch, Z. Qiu, and K. Bertoldi, "A comparative analysis of numerical approaches to the mechanics of elastic sheets", Journal of the Mechanics and Physics of Solids **79**, 92–107 (2015).

[12] M. Smith, *Abaqus/cae 2018 user's manual* (Dassault Systèmes Simulia Corp, United States, 2018).

[13] H. Pham Dinh, V. Démery, B. Davidovitch, F. Brau, and P. Damman, “From Cylindrical to Stretching Ridges and Wrinkles in Twisted Ribbons”, Physical Review Letters **117**, 104301 (2016).

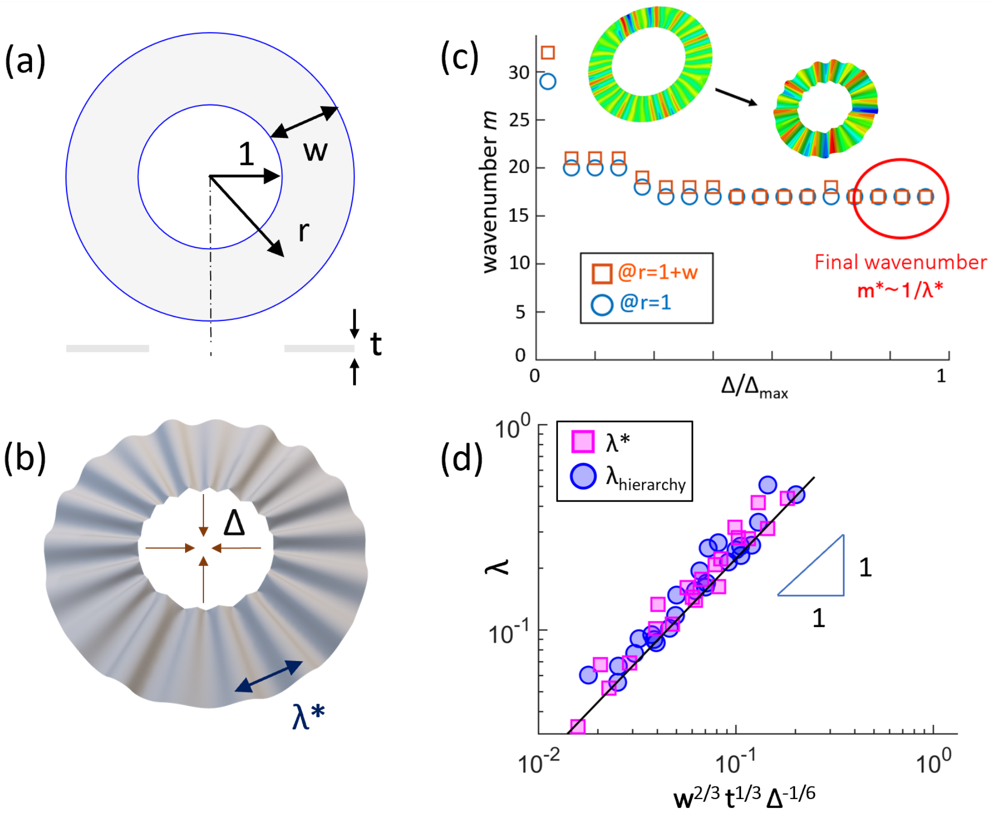

Figure 3.1: Geometry of the Inner Lamé radially wrinkled system, and selected wavelengths in its numerical implementation. (a) A schematic diagram of the flat annulus, showing its geometric parameters: radial distance r, width w and (in cross-section) thickness t. We take the inner radius as unity. (b) An example of a deformed configuration, showing the displacement Δ and the wrinkle wavelength λ^*, measured at the outer boundary, which we wish to predict. (c) shows representative data for the evolution of the wavenumber (i.e. the number of wrinkles) against normalised contraction $\Delta/\Delta_{\mathrm{max}}$, measured at both inner ($r = 1$) and outer ($r = 1+w$) boundaries. m decreases until it saturates to a value $m^* \equiv 2\pi(1+w)/\lambda^*$. (d) shows data collapse on a log-log scale of measured λ^*, along with $\lambda_{\mathrm{hierarchy}}$ for the pinned version (see Sec. 3.3.3), onto the predicted scaling law given in Eq. 3.5. The data are for multiple numerical annuli with varying w, t and Δ. The black line represents the best-fit equation: $y = 2.2\,x$ (log-log scale). Henceforth, we term this the "wrinklon line" and depict it using λ^*.

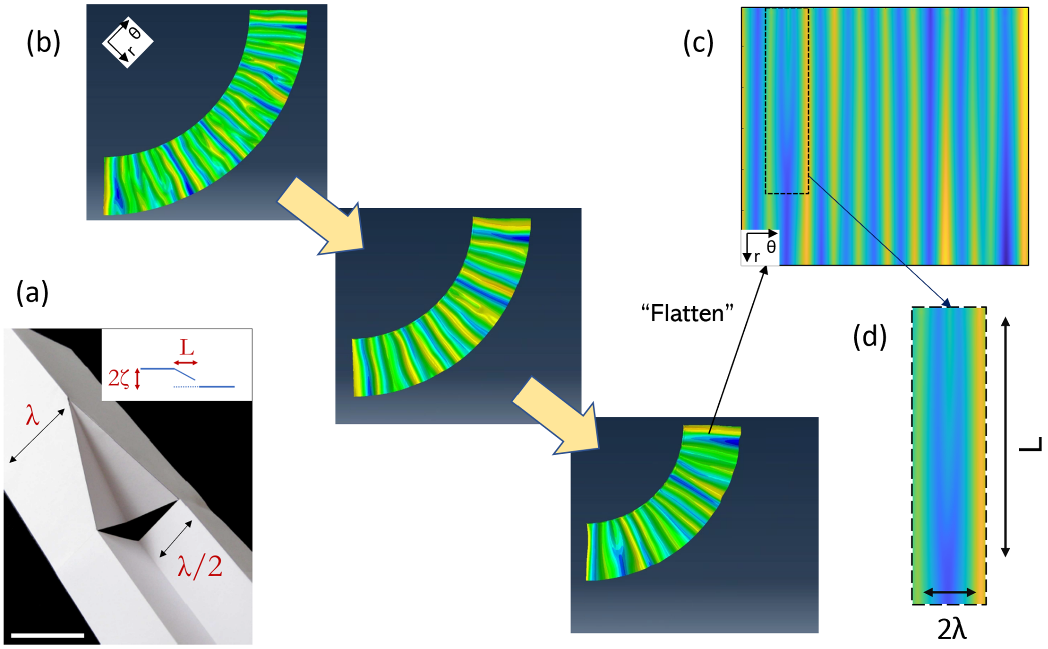

Figure 3.2: Wavelength coarsening and wrinklons (see Sec. 3.3.1). (a) An origami paper model of a Y-shaped wrinklon joining, wavelength $\lambda \to 2\lambda$ (measured in-plane; half-wavelengths shown), revealing the nature of its stretching (image modified from [9]; scale bar is 5 cm). The gap in the shape shows that a continuous sheet requires longitudinal stretching to accommodate the wrinklon (see Sec. 3.3B). (inset) A schematic diagram of the mid-line of the sheet (in blue), showing its vertical amplitude ζ and length L, used in Eq. 3.1. (b) An illustrative example of wavelength coarsening in the inner Lamé system (for $w = 0.33, t = 6.67 \times 10^{-4}$). The three snapshots are for the bottom-right quadrant of the annulus (coloured by height) taken at $\Delta \approx 0.07, 0.15, 0.23$ resp. (c) To visualise the wrinkling pattern with greater clarity, we 'flatten' the polar coordinates, so that the height profile can be plotted in a rectangular matrix form (same colours, but different colour map). Here, the top edge is the inner boundary. (d) A close-up of a wrinklon in (c), joining wavelengths $\lambda \to 2\lambda$, of longitudinal size L.

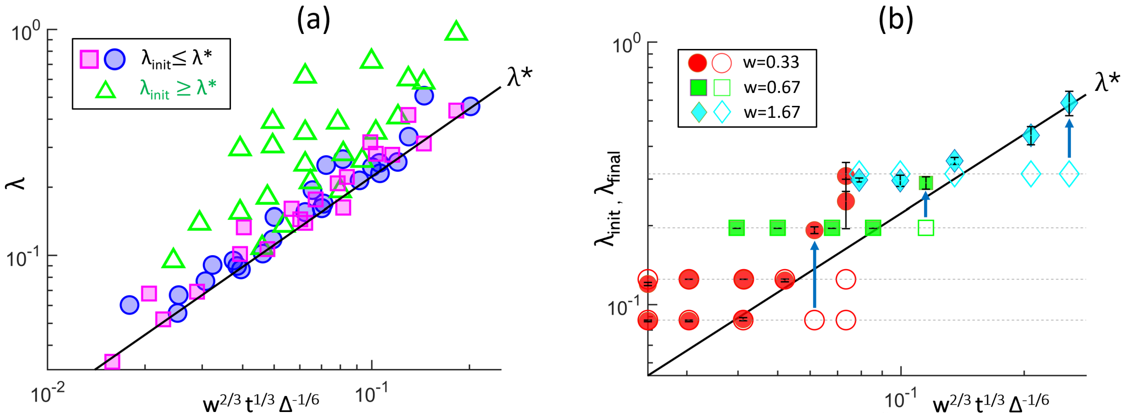

Figure 3.3: Effect of varying the initial wavelength λ_{init}. (a) The data points (in blue and magenta) and best-fit 'wrinklon line' from Fig. 3.1c, having $\lambda_{\text{init}} \leq \lambda^*$, are overlaid with new sample points (in green) that start from a *biased* flat state with a perturbation of wavelength $\lambda_{\text{init}} \geq \lambda^*$. These biased samples show little to no coarsening. (b) We see the difference in coarsening behaviour clearly by plotting both λ_{init} (empty symbols) and the final wavelength λ_{final} (solid symbols) for some selected samples. Here, we fix λ_{init} and width w, and vary the thickness t, thereby creating a horizontal row of empty symbols for given λ_{init}. We plot λ_{init} and λ_{final} with the same w, t and Δ, so that any coarsening is noticeable by a vertically upward shift of the solid symbol (some arrows drawn for indication). We see a clear transition from non-coarsening to coarsening behaviour as we cross the black wrinklon line. The error bars denote standard error from averaging over all the wrinkles.

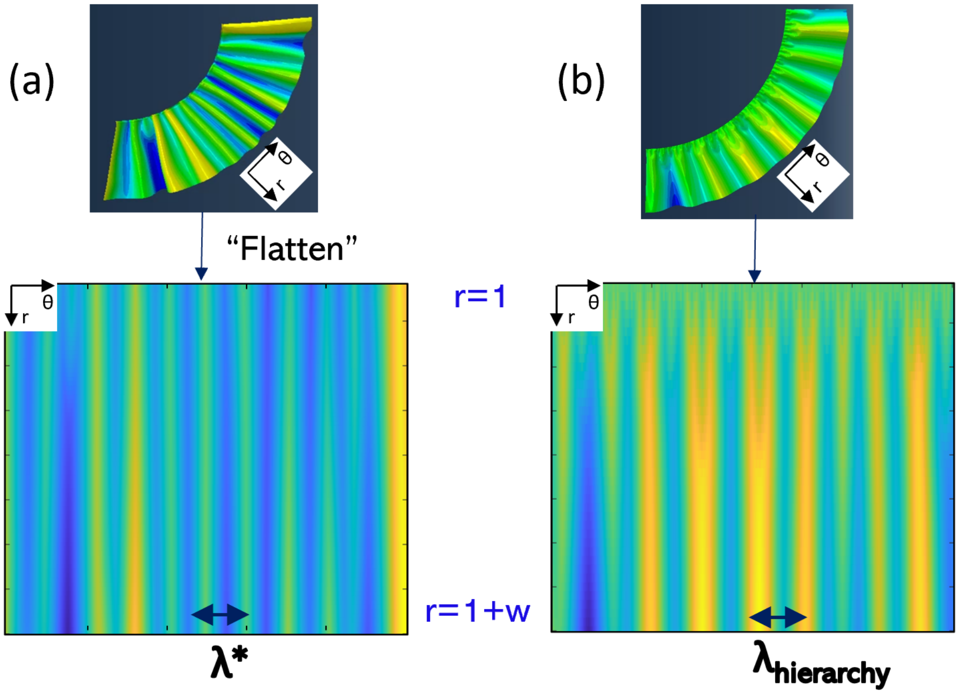

Figure 3.4: Contrasting wrinkled morphologies but similar outer wavelengths, for two different boundary conditions at the inner boundary ($r = 1$) (see Sec. 3.3.3). Data are for the same representative sample used in Fig. 3.2b ($w = 0.33$, $t = 6.67 \times 10^{-4}$). The top row shows the bottom-right quadrant of the deformed annulus in both cases (coloured by height). The bottom row shows the same height profile, but flattened into a rectangular matrix form, as in Fig. 3.2 above. (a) The "inner Lamé" boundary condition, the subject of this paper, which allows free vertical displacement at $r = 1$. This leads to near-uniform radial wrinkling, with wavelength λ^* at the outer boundary ($r = 1 + w$). (b) A pinned boundary condition that prohibits vertical displacement at $r = 1$. This leads to a spatial wrinkle hierarchy, that terminates with the coarsest wavelength $\lambda_{\text{hierarchy}}$ at $r = 1 + w$.